Finanziato dall'Unione europea NextGenerationEU
Ministero dell'Università e della Ricerca
Italiadomani PIANO NAZIONALE DI RIPRESA E RESILIENZA

multi-Risk sciEnce for resilienT commUnities undeR a changiNg climate Codice progetto MUR: **PE00000005** – **B83C22004820002**

Deliverable title: Report with graphs and data tables of pre-eruptive parameters and magma-rock interaction from laboratory and experimental studies

Deliverable ID: DV 3.3.1

Due date: 31/03/2026

Submission date: 31/03/2026

AUTHORS

Raffaello Cioni, Pietro Gabellini, Lorella Francalanci, Simone Tommasini (UNIFI); Cristina Perinelli, Mario Gaeta, Danilo Palladino (UNIROMA1); Pooria Ebrahimi, Daniele Morgavi, Paola Petrosino (UNINA)

1. Technical references

Project Acronym	RETURN
Project Title	multi-Risk sciEnce for resilienT commUnities undeR a changiNg climate
Project Coordinator	Domenico Calcaterra UNIVERSITA DEGLI STUDI DI NAPOLI FEDERICO II domcalca@unina.it
Project Duration	December 2022 – November 2025 (36 months)

Deliverable No.	DV 3.3.1
Dissemination level*	
Work Package	WP3 – Hazard and expected impact of explosive volcanoes
Task	T 3.3.1 - Pre-eruptive physico-chemical magma characteristics
Lead beneficiary	UNIFI
Contributing beneficiary/ies	UNIFI, UNIROMA1, UNINA

* PU = Public

PP = Restricted to other programme participants (including the Ministry Services)

RE = Restricted to a group specified by the consortium (including the Ministry Services)

CO = Confidential, only for members of the consortium (including the Ministry Services)

Document history

Version	Date	Lead contributor	Description
0.1	14/03/2026	Raffaello Cioni (UNIFI)	First draft
0.2			Critical review and proofreading
0.3			Edits for approval
1.0			Final version

2. ABSTRACT

Characterization of pre-eruptive physico-chemical characteristics of magma is basic to the understanding of the main processes which drive an eruption, from mechanisms of eruption trigger to the definition of the eruptive style, which on turn determines the type of hazard and extent of impact on the territory. Magma evolves in deep or shallow reservoirs through different mechanisms, from classical crystal fractionation, chemical mixing or physical mingling with different silicatic melts, up to interaction with solidifying melts or even host rocks. The research performed in the framework of Task 3.3.1 “Pre-eruptive physico-chemical magma characteristics” addresses all these different processes through the study of selected past eruptions at Vesuvius, Campi Flegrei, Stromboli and other Quaternary potassic volcanoes of Central and Southern Italy. Two different approaches were followed in the research; 1- the study of the products of past explosive eruptions, aimed at defining the role of the compositional variations observed in the magma in affecting eruptive dynamics; 2- application of methods of experimental petrology to assess how the physico-chemical conditions of magma crystallization and solidified magma reactivation can influence eruptive style.
The research has produced a wealth of new data that are only partially presented and described in this report, and that are available on request to the authors.

3. Table of contents

List of Tables

List of Figures

4.UNIFI

4.1 Precursors to large explosive activity of Vesuvius from the study of the opening phases of past Plinian eruptions

Activity goals. Stratigraphical, textural, geochemical and petrographical data of the first erupted deposits of Plinian eruptions from Vesuvius help to define modalities and timing of pre- and syn-eruptive magma ascent and eruption trigger, and to constrain the expected measurables in case of reactivation.

Main results. The onset of a large explosive volcanic eruption is generally characterized by a weak transient activity. The products of this opening phase(s) of the eruptions are confined to thin proximal beds of small volume and limited dispersal. The juvenile material erupted in the opening phase provides a unique record of pre- and syn-eruptive processes and preserves key information on eruption triggering and dynamics during magma ascent. The study of these products can provide insights into precursory phenomena and assumes a key role for the interpretation of monitoring signals at high-risk volcanoes. We have performed a detailed study of the products from the opening phases of the Avellino and of the CE 79 Pompeii Plinian eruptions of Somma-Vesuvius (Italy), well preserved in their proximal deposits.

The deposits of the opening phase of Avellino eruption show a large textural and compositional variability of the juvenile material, which depicts a complex process of magma extraction at the onset of the eruption. During this very short initial phase of the eruption, phonolitic pumice with a composition similar to that erupted during the intermediate phase of the eruption were ejected, together porphyritic, glass-bearing dense blocks of variable composition (Fig. 4.1.1). Geochemical, textural, and geobarometric data (Figs. 4.1.2, 4.1.3) on all these products reveal the presence of a magma body at shallow depth that cooled and partially crystallised under different conditions compared to the main, deeper, and larger magma reservoir feeding the paroxysmal phases of the eruption (Fig. 4.1.4). Elemental diffusion chronometry on clinopyroxene from juvenile material suggests that magma movement toward the shallow reservoir anticipated the eruption by a maximum of about 100 years, while the arrival of a last mafic input into the shallow magma body can be confined to only a few years before the eruption (Table 4.1.1).

Conversely, the initial phase of the Pompeii eruption was marked by the contemporaneous ejection of phonolitic White Pumice and tephri-phonolitic Grey Pumice (Figs. 4.1.5, 4.1.6). This is interpreted as the early destabilization of a diffusive interface placed in a compositionally stratified magma reservoir, at the boundary between phonolitic and tephri-phonolitic magma, possibly triggered by the arrival of deep mafic magma batch(es) which only briefly anticipated the eruption. This mechanism induced mixing processes and the contemporaneous withdrawal of magma from the uppermost and the lower portions of the magmatic reservoir, resulting in a large compositional and textural variability of products emitted during the AD 79 opening phase.

All the data are available on request to the authors.

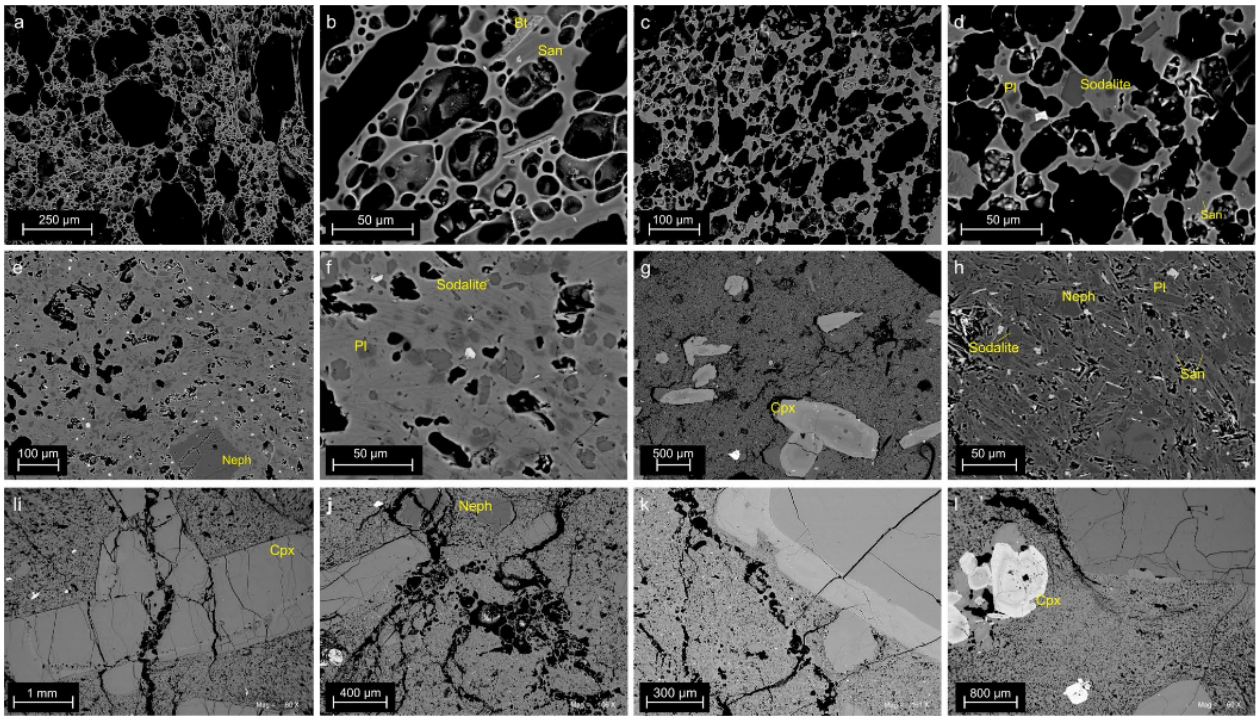

Fig. 4.1.1 SEM images obtained from thin sections of the juvenile material erupted during the Avellino opening phase. a Groundmass texture of - WPEU1. Larger bubbles are generally with elliptical and irregular shapes; smaller bubbles (< 100 µm) are commonly spherical. Sometimes vesicles are stretched in a preferential direction. b Magnification of the groundmass texture of - WPEU1. Microlite of biotite and sanidine are set in the glassy matrix. c Groundmass texture of scoriae. d Magnification of the groundmass texture of scoriae: coarser and more irregular vesicles than that of - WPEU1 are observed. The groundmass is characterised by a mixture of glass and microlites of acicular sanidine, euhedral sodalite, plagioclase, and amphibole (white small fragments in the left). e, f Groundmass texture of low vesicular clasts. Scarce vesicles and the high microlite content characterise the matrix groundmass. Microlites mainly consist of acicular sanidine (light grey), sodalite, nepheline, plagioclase, mafic mineral phases, and oxides. g Texture of the mafic type of dense clast. Phenocrysts of clinopyroxene are set in a highly crystallised groundmass. h Detail of image g. Acicular sanidine, tabular plagioclase, nepheline, sodalite, and acicular mafic phase (in white) characterised the groundmass. i, j, k, l BSE (back-scattered) images of T1 blocks showing the peculiar texture recognised in this kind of blocks. Fracture zones with large vesicles and glassy texture cut through the groundmass and phenocrysts as results of local decompression and deformation of T1 blocks.

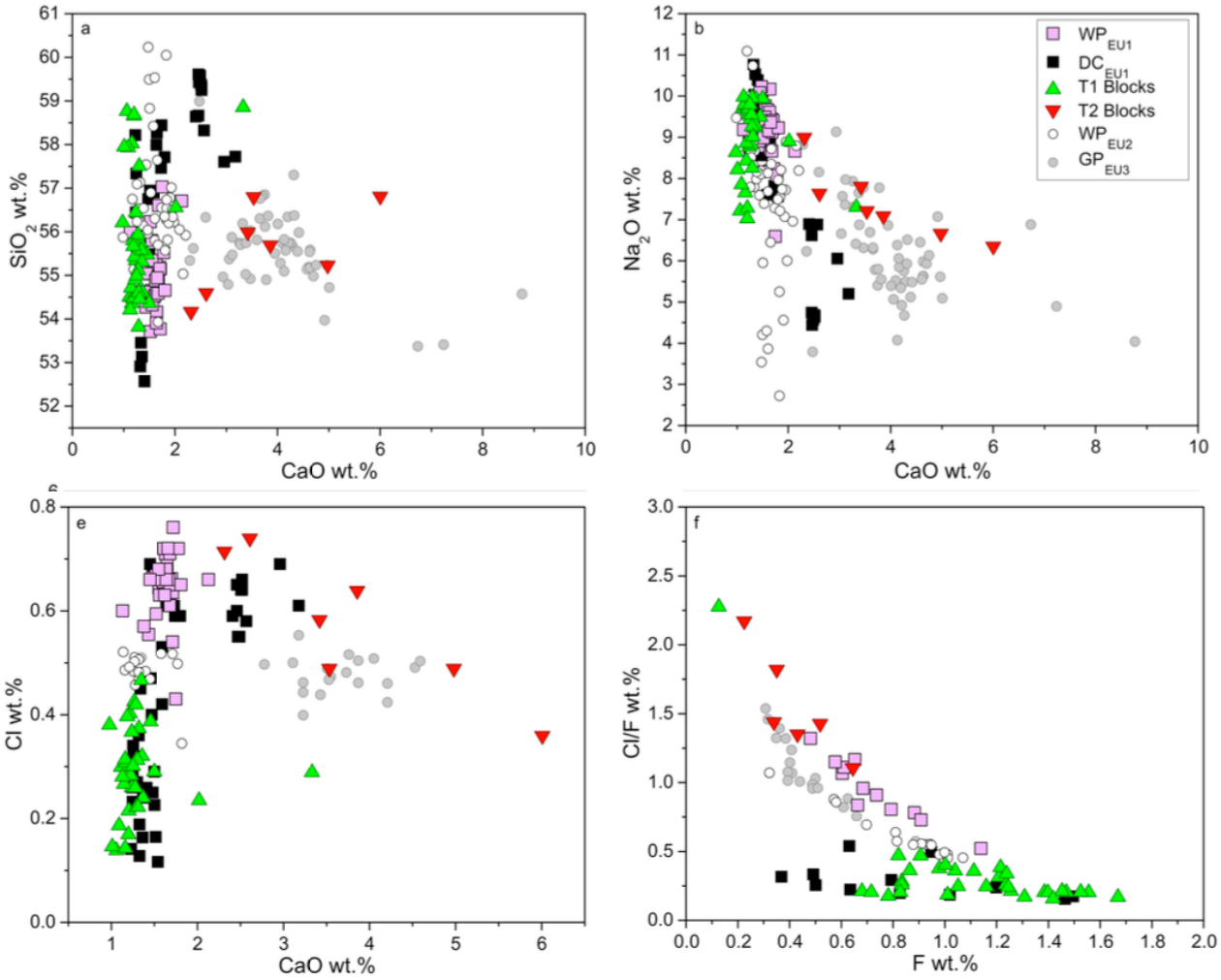

Fig. 4.1.2 Groundmass glass compositions studied in this work, along with chemical analysis of glass of Plinian white pumices, WPEU2, and Plinian grey pumices, GPEU3, data from Santacroce et al. (2008). a–d CaO content versus SiO2, Na2O, FeO, and K2O contents. Major element concentration plots record significant similarity between T2 blocks (in red) and GPEU3 (in grey) glass compositions. Such similarity is marked again when plotting volatiles content, Cl, against CaO concentrations (e). In f, the Cl/F ratio shows a regular variation, with WPEU1 and T2 blocks showing a trend very close to that shown by WPEU2 and GPEU3 of the Plinian phase. As demonstrated by the concentration of major elements, one of the glasses stands out from the others in terms of its volatile concentrations. Specifically, it has lower concentrations of F but comparable contents of Cl to the other glasses from T1 blocks.

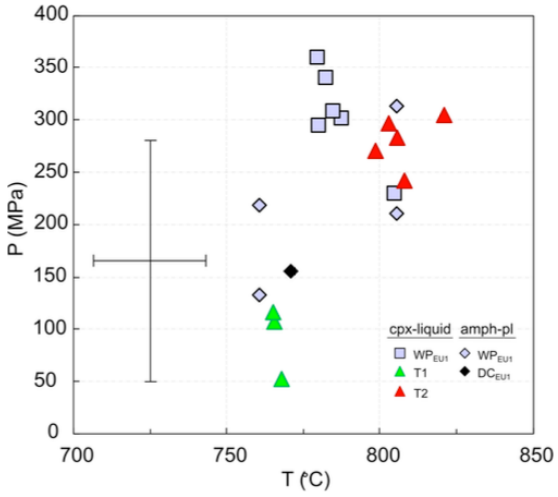

Fig. 4.1.3 Temperature and pressure estimates from the different clast types belonging to the basal deposit of the Avellino eruption following the clinopyroxene-liquid models from Masotta et al. (2013). In the bottom left, the standard error estimates of both thermometer (equation Talk2012) and barometer (equation Palk2012) from Masotta et al. (2013) is reported. Pressures modelled applying the amphibole-liquid barometer of Molina et al. (2015,2021; SEE: ± 150 to ± 230 MPa) in dense clasts, DCEU1, at given temperatures of 770 °C and WPEU1 at 760 and 805 °C are reported for comparison.

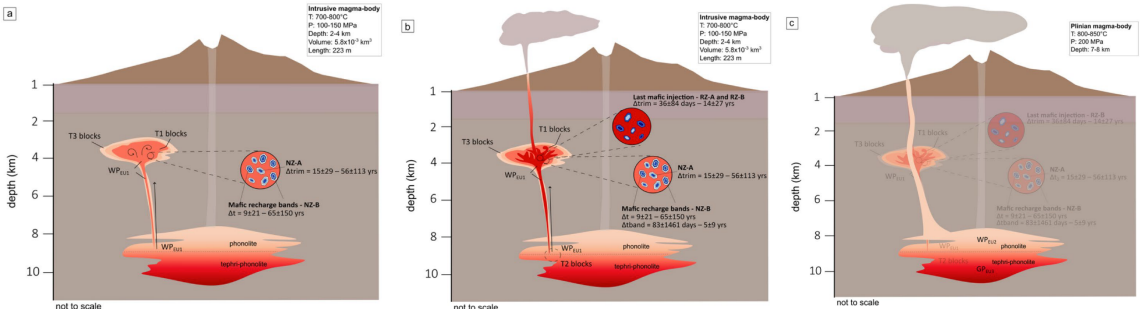

Fig. 4.1.4 Proposed model of mid-term pre-eruptive conditions and opening phase of the Avellino eruption

Sample	Crystal	Type	Boundary	Mg#	T °C	T environment	Δt	Timescale (years)	1sd (years)
AVD9	PX10	RZ-B	band-rim	80	1052	high T	Δt_2	0.06	0.11
AVD9	PX9	RZ-B	core-rim	67	1044	high T	Δt_2	0.10	0.20
AVD9	PX4	RZ-B	core-rim	65	977	high T	Δt_2	1.10	2.10
AVD9	PX1	RZ-A	core-mantle	70	1007	high T	Δt_2	4.21	7.85
AV_B	PX13	RZ-B	core-rim	51	902	high T	Δt_2	13.90	27.30
AV_B	PX5	NZ-A	band-rim	51	890	low T	Δt_2	15.10	28.90
AVD9	PX8	NZ-A	band-rim	49	890	low T	Δt_2	25.70	50.30
AV_B	PX10	NZ-A	band-rim	46	872	low T	Δt_2	31.94	62.39
AVD1	PX12	NZ-A	band-rim	37	824	low T	Δt_2	56.25	113.56
AVD1	PX9	NZ-A	band-rim	42	849	low T	Δt_2	1384.36	2869.50
AVD9	PX3	NZ-B1	core-DB-rim	47	918	low T	total	12.90	26.20
AVD9	PX3	NZ-B1	core-DB-rim	70	1008	high T	Δt_4	0.19	4.90
AVD1	PX5	NZ-B1	core-DB-rim	51	889	low T	total	52.92	55.34
AVD1	PX5	NZ-B1	core-DB-rim	61	956	high T	Δt_4	4.85	9.44
AVD9	PX7	NZ-B1	core-DB-rim	45	938	low T	total	53.70	124.40
AVD9	PX7	NZ-B1	core-DB-rim	68	994	highT	Δt_4	1.34	2.55
AVD9	PX6	NZ-B1	LB-DB	52	908	high T	Δt_4	15.60	30.80
AVD9	PX6	NZ-B1	LB-DB	44	860	low T	Δt_4	122.10	249.80
AVD1	PX7	NZ-A	core-band	70	971	high T (t min)	Δt_4	0.44	0.85
AVD1	PX7	NZ-A	core-band	64	897	low T (t max)	Δt_4	5.30	10.56
AVD9	PX2	NZ-B2	core- mantle	61	955	high T	Δt_4	1.69	3.54
AVD9	PX2	NZ-B2	core- mantle	37	822	low T (t max)	Δt_4	211.40	464.60
AVD9	PX2	NZ-B2	DB-rim	37	822	low T	Δt_2	381.90	782.20
AV_B	PX7	NZ-B1	core-rim	59	934	high T (tmin)	Δt_4	4.10	7.90
AV_B	PX7	NZ-B1	core-rim	52	904	low T (t max)	Δt_4	11.55	22.33
AVD1	PX11	NZ-B1	core-mantle	62	960	high T (t min)	Δt_4	4.79	9.18
AVD1	PX11	NZ-B1	core-mantle	44	824	lowT (t max)	Δt_4	328.71	663.48
AV_B	PX4	NZ-A	core-band	60	950	high T (tmin)	Δt_4	69.90	130.72
AV_B	PX4	NZ-A	core-band	51	898	low T (t max)	Δt_4	297.40	577.60

Table 4.1.1. Timescales estimates from diffusion chronometry using the NIDIS model (Petrone et al., 2016)

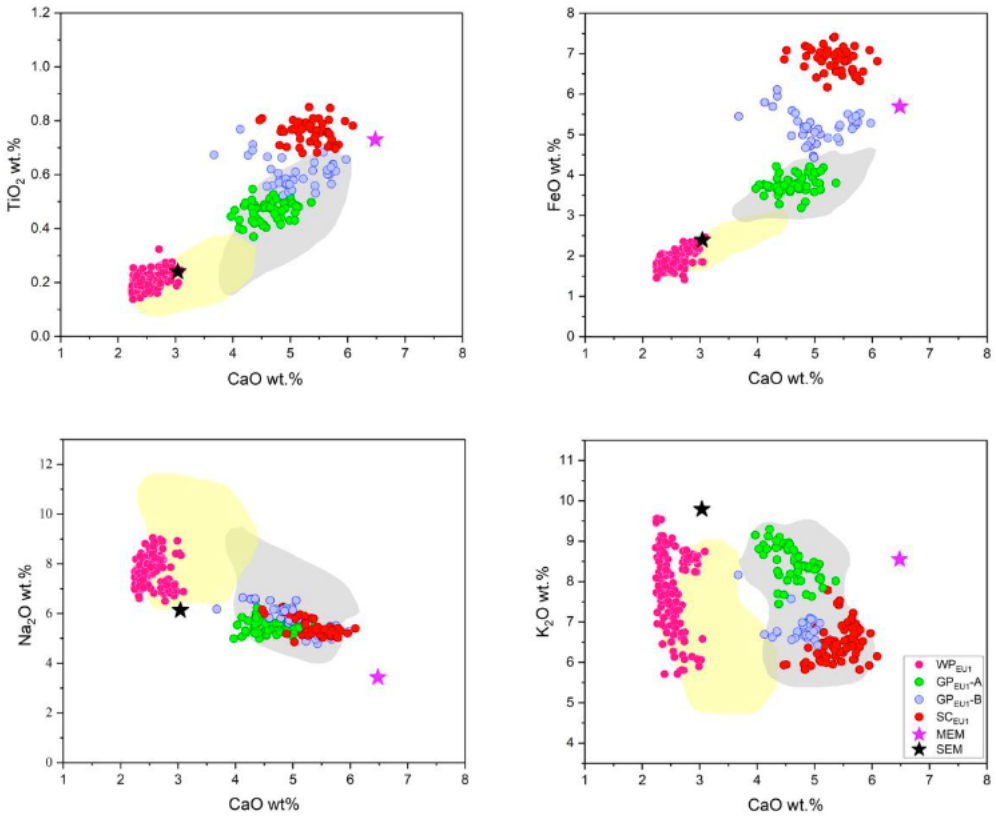

Fig. 4.1.5 CaO wt.% vs selected major element compositions of WPEU1, GPEU1, GP-A and SC matrix glasses from the opening phase of the AD 79 Pompeii eruption. Matrix glasses chemical variations are compared with the SEM and MEM estimated from Cioni et al., 2005. White Plinian pumice (WPp) and grey Plinian pumice (GPp) fields are from literature data (Cioni et al., 2005; Melluso et al., 2022; Wotzlaw et al., 2022).

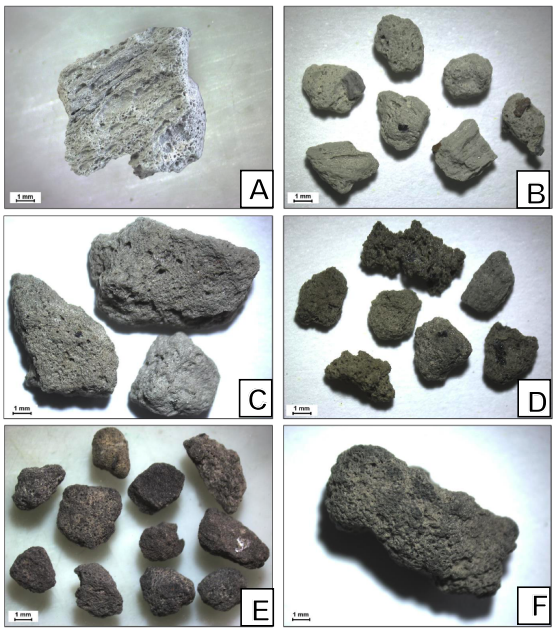

Fig. 4.1.6 Different types of juvenile material in the opening phase of the AD79 eruption. A. WP (White Punice) with tubular, highly vesicular glassy texture. B. WP clasts; both microvesicular and tubular clasts are evident. C. Gray Pumice (GP) with both spongy and microvesicular external surfaces. D. Few mafic mineral phases, reaching maximum size of 1 mm (GP in the bottom right), are evident. E, F. Dark low vesicular scoriae found in the thin basal layer of the AD 79 eruption. Samples have both spherical to elongated shape, sometimes presenting sub-angular external surfaces. Vesicles vary from small to coarse and are in general homogeneously distributed.

,

4.2 *Isotopic and petrological monitoring of the Stromboli activity, and new constraints on the architecture of the plumbing system*

Activity goals. The assemblage of large, stratigraphically and volcanologically constrained datasets of isotopic data on bulk rock and matrix glasses, and of compositional data of clinopyroxene (Tables 4.2.1, 4.2.2), are used to constrain changes in magma genesis and thermo-baric conditions of magma crystallization in the deep and shallow plumbing system of Stromboli volcano, aimed at interpreting the present state and defining the expected future changes of this volcanic system.

Main Results. A large dataset of Sr-Nd isotope ratios on whole rocks and matrix glasses has been collected for the products of different styles of activity of Stromboli volcano, from normal Strombolian, to effusive, up to paroxysmal eruptions. The analysed samples consist of scoriae and lavas (representative of degassed, highly porphyritic magma - hp-magma) and pumices (volatile-rich magma and with low phenocryst content - lp-magma), continuing and completing the isotopic dataset already available and published, which reported data since the beginning of 1900 CE up to 2007 CE (e.g., Francalanci et al. 1999, 2004, 2005, 2012; Landi et al. 2009; Bragagni et al. 2014) (representative analyses are reported in Table 4.2.2). In these data, Nd isotopes are nearly constant, Sr isotopes remained constant up to about 1980 CE for decreasing afterwards in the different analysed lithotypes. In the new isotopic data, collected on the products of the most recent activity, the observed change in the Sr isotope trend show a new increase, which is particularly accentuated in the lp-magma. This suggests variations in the plumbing system dynamics linked to nearly parallel changes in the parental magmas, determined by a heterogeneous and still active mantle source.

New Electron Microprobe analyses of 220 clinopyroxenes (596 data points) from 69 samples have been collected, covering the eruptive periods of the last 110 yrs of activity, with most of the analyses relative to the III millennium and including the normal Strombolian activity, the effusive activity, the major eruptions, and the paroxysmal eruptions. Representative analyses of clinopyroxenes are reported in Table 4.2.1 and the entire dataset can be available on request. In addition to these new analyses, compositional data from a number of previous published data, for a total of 1595 high-quality analyses of 328 clinopyroxenes and 120 samples were selected and used to build a reference dataset which complements the eruptive activity of the last 110 yrs, together with a Middle Ages paroxysmal eruption of 1456 CE. The overall clinopyroxene dataset shows interesting mineral variations linked to the different types of activity, as the different trends shown in the Mg#-Al2O3 diagram (Fig. 4.2.1). Moreover, this dataset was used to yield pressure and temperature estimates using a novel clinopyroxene-only geothermobarometer based on Feedforward Neural Networks (FNN) machine learning technique (GAIA, Chicchi et al., 2023) (Fig. 4.2.2). The data are used to constrain the thermo-barometric conditions of magma ponding in the deep and shallow plumbing system, trying to differentiate different clinopyroxene crystallization phases by applying the geothermo-barometer to different zones of the crystals (core, intermediate, rim).

Fig. 4.2.1 - Diagram of Mg# versus Al_{tot} (atoms per formula unit) for the analysed clinopyroxenes of the present-days activity of Stromboli, showing different trends for the augites (blue, Mg# lower than 80) and diopsides (red, Mg# higher than 80). The main group of augites, with Mg# between 72 and 79, represent the shallow hp-magma reservoir, whereas augites at lower Mg# are antecrysts from a previous activity. Diopsides describe two trends at different Al enrichment: the high-Al trend is formed by diopsides of paroxysms, whereas the low-Al trends is formed by diopsides in reaction with augitic cores or crystallised by hp-lp mixed melts and found in the products of the other types of eruptions.

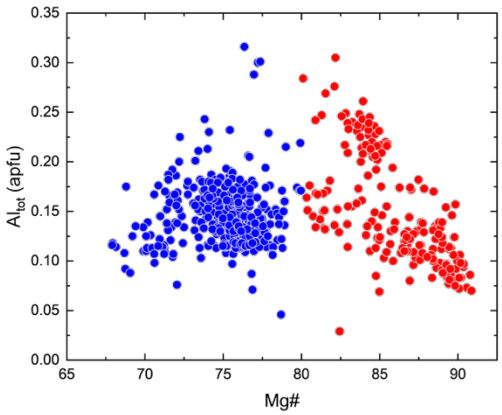

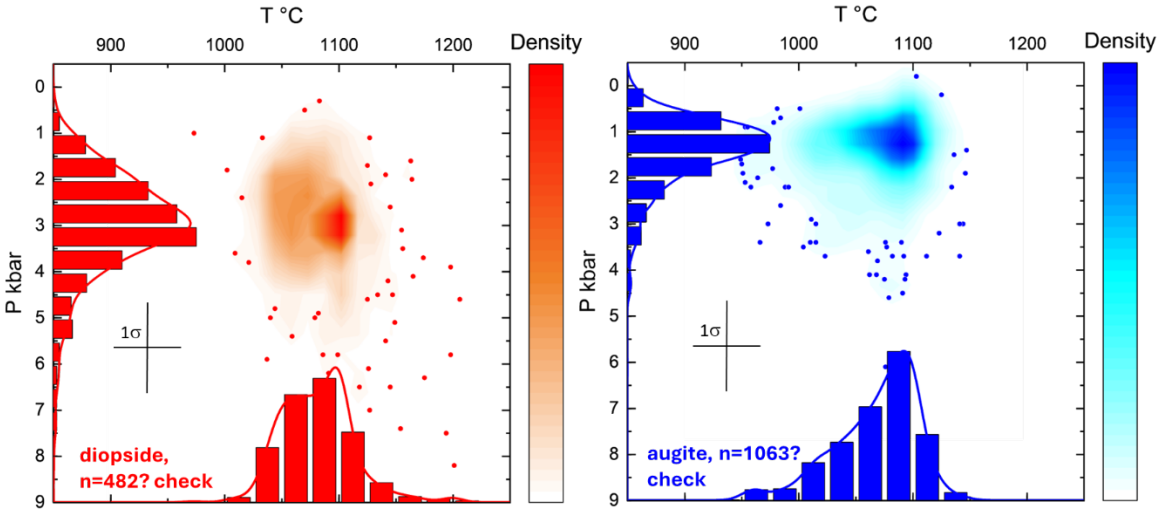

Fig. 4.2.2 - The results of the P-T calculations are reported in the 2D Kernel density distribution diagrams, subdivided between diopside, crystallising in the lp magma, and augite, crystallising in the hp magma. Diopside (Fig. 2a) yields a major peak in pressure between 2.5 and 3.5 kbar, with a tail to lower pressure, down to 1.0-1.5 kbar. A minor tail to higher pressure (3.5-5.5 kbar) is present as well. In contrast, augite (Fig. 2b) yields an almost gaussian distribution with a peak at pressure of 1.0 -1.5 kbar, and nearly symmetrical high and low-P tails. Despite the two distinct peaks discriminating the main pressure of crystallization of diopside and augite, the observed tails indicate a continuum of augite and diopside crystallization from about 4.5 kbar to 0.5 kbar, consistent with a network of channels interconnecting multiple magma ponding and storage levels. In terms of temperature, diopside and augite yield similar ranges. Diopside has an almost gaussian distribution of crystallization temperature between 1050 and 1100°C , with tails from 1100-1150°C up to 1025-1050°C. Augite has an asymmetric distribution of crystallization temperature, with a peak at 1075-1100°C and a significant tail to lower temperature, up to 950°C.

Table 1 - Major element composition of selected clinopyroxenes

Eruption	29/3	1929	11/9	11/9	6/9	6/9	6/9	10/9	4/9	4/9	4/9	23/8	23/8	6/9
date	1914		1930	1930	1994	1994	1994	1995	1996	1996	1996	1998	1998	2000
Activity	NA	E	P	P	NA	NA	NA	NA	ME	ME	ME	ME	ME	ME
Sample	ES10	ES281	ES204	ES204	STR09/9 4a	STR09/9 4a	STR09/9 4a	STR09/9 5b	STR09/9 6d4	STR09/9 6d4	STR09/9 6e2	STR08/9 8i	STR08/9 8L1	STR9/00 f
Lithotype	Scoria	Lava	Scoria	Scoria	Scoria	Scoria	Scoria	Scoria	Pumice	Pumice	Scoria	Pumice	Scoria+ Pumice	Pumice
Zone	out rim	rim	core	rim	core	out core	rim	core	micr cor	mic core	out rim	mic core	out rim	ner rim
Major Elements														
SiO2	50.35	53.51	50.36	52.16	50.23	53.38	50.12	50.13	50.17	50.08	50.92	51.62	50.58	50.82
TiO2	0.8	0.28	0.87	0.34	0.62	0.26	0.83	0.82	0.98	0.57	0.8	0.67	0.72	0.63
Al2O3	3.14	2.25	3.74	3.01	2.97	1.93	3.25	3.45	3.84	4.78	3.05	3.18	5.42	3.75
Cr2O3	0.06	0.37	0.06	0.21	0.05	0.65	0.05	0.02	0	0.07	0.04	0	0.18	0.08
Fe2O3	3.6	-	2.35	2.04	2.67	-	3.02	4.37	3.9	2.64	2.41	1.29	0.8	2.18
FeO	5.48	4.4	6.28	3.06	6.12	3.22	5.64	5.54	6.89	3.19	6.16	7.84	4.38	4.47
MnO	0.21	0.12	0.19	0.14	0.26	0.12	0.2	0.28	0.3	0.1	0.24	0.25	0.1	0.14
MgO	14.92	17.23	14.84	16.87	14.98	17.21	14.57	15.22	14.39	15.46	14.81	15.28	15.3	15.02
CaO	21.01	21.69	20.79	22.19	20.26	22.63	21.12	20.35	20.08	22.16	21.25	19.82	22.02	22.18
Na2O	0.37	0.21	0.31	0.21	0.34	0.19	0.39	0.35	0.47	0.25	0.34	0.34	0.25	0.33
tot	99.94	100.06	99.79	100.23	98.5	99.59	99.19	100.53	101.02	99.3	100.02	100.29	99.75	99.6
Chemical formula														
Si	1.871	1.95	1.871	1.902	1.89	1.951	1.876	1.854	1.853	1.851	1.889	1.907	1.858	1.881
Al	0.129	0.05	0.129	0.098	0.11	0.049	0.124	0.146	0.147	0.149	0.111	0.093	0.142	0.119
Mg	0.827	0.936	0.822	0.917	0.84	0.938	0.813	0.839	0.792	0.852	0.819	0.841	0.838	0.829
Fe2	0.17	0.134	0.195	0.093	0.193	0.098	0.176	0.171	0.213	0.099	0.191	0.242	0.135	0.138
Fe3	0.101	0	0.066	0.056	0.076	0	0.085	0.122	0.108	0.073	0.067	0.036	0.022	0.061
Al	0.008	0.046	0.035	0.032	0.022	0.034	0.019	0.004	0.02	0.06	0.022	0.045	0.093	0.045
Ti	0.022	0.008	0.024	0.009	0.018	0.007	0.023	0.023	0.027	0.016	0.022	0.019	0.02	0.018
Cr	0.002	0.011	0.002	0.006	0.001	0.019	0.001	0.001	0	0.002	0.001	0	0.005	0.002
Mn	0.007	0.004	0.006	0.004	0.008	0.004	0.006	0.009	0.009	0.003	0.008	0.008	0.003	0.004
Ca	0.836	0.847	0.828	0.867	0.817	0.886	0.847	0.806	0.795	0.878	0.845	0.784	0.867	0.88
Na	0.027	0.015	0.022	0.015	0.025	0.013	0.028	0.025	0.034	0.018	0.024	0.024	0.018	0.024
Classification														
Fs	14.30	7.17	13.93	7.92	14.30	5.30	13.89	15.49	17.24	9.19	13.78	14.95	8.58	10.64
Wo	43.10	44.09	43.18	44.75	42.24	46.01	43.94	41.41	41.44	46.08	43.77	41.03	46.48	46.01
En	42.60	48.73	42.89	47.33	43.46	48.69	42.17	43.10	41.32	44.73	42.45	44.02	44.94	43.35
Mg#	74.8	87.2	75.5	85.7	75.2	90.2	75.3	73.5	70.6	83.0	75.5	74.6	84.0	80.3
GAIA geoTP														
P kbar	1.4	3.1	1.4	2.7	1.6	2.8	0.9	1.4	2.6	3.9	0.8	3.8	3	0.2
1sd	0.4	0.5	0.4	0.4	0.4	0.5	0.4	0.3	0.6	0.6	0.3	0.7	0.5	0.4
T °C	1085	1050	1015	1061	982	1100	1093	1082	1046	1042	1063	1069	1059	1115
1sd	32	13	12	15	9	9	19	28	20	8	19	26	24	15

Table 4.2.1 Major elements composition of selected pyroxenes. Chemical formula recalculated on the basis of 4 cations and Fe2+/Fe3+ was adjusted to maintain charge balance. Geothermobarometric estimates following GAIA (Chicchi et al., 2023).

Augite - Diopside; type of activity - NA: normal activity; E: effusive; P: paraxysm; ME: major eruption.

Table 1 - continued

Eruption	6/9	28/12	28/12	15/1	15/1	5/4	5/4	20/7	20/7	20/7	9/1	9/1	15/3	10/1
date	2000	2002	2002	2003	2003	2003	2003	2003	2003	2003	2005	2005	2007	2010
Activity	ME	E	E	E			P	E		E	ME		P	NA
Sample	STR9/00	STR12/0	STR120	STR150	STR150	STR050	STR050	STR200	STR200	STR200	STR090	STR090	STR	STR100
	f	2a	2a	103v	103v	403q	403q	703	703	703	105	105	150307	110b
Lithotype	Pumice	Lava	Lava	Lava	Lava	Pumice mingled	Pumice mingled	Lava	Lava	Lava	Scoria	Scoria	Pumice	Scoria
Zone	rim	core	ner core	core	rim	core	outer rim	core	rim	ıter core	core	outer rim	rim	rim
Major Elements														
SiO2	50.33	51.14	50.6	52.75	50.12	50.67	50.61	50.22	50.48	52.76	50.71	51.47	49.88	49.86
TiO2	0.93	0.79	0.92	0.51	1.06	0.69	0.56	0.98	0.86	0.25	1.21	1.07	0.74	0.88
Al2O3	3.81	3.39	4.3	2.72	4.16	3.5	4.64	4.17	3.3	2.65	4.07	3.58	5.61	4.09
Cr2O3	0	-	0.09	0.1	0.04	-	0.13	0.03	0.04	0.72	0.04	0.02	0.25	0.1
Fe2O3	2.23	-	1.22	1.17	2.3	3.53	2.64	2.24	2.98	2.1	2.53	2.17	2.35	4.45
FeO	7.06	5.87	7.51	3.93	6.48	6.7	3.1	6.01	5.49	1.6	6	6.17	2.93	3.74
MnO	0.26	0.18	0.16	0.1	0.18	0.37	0.08	0.16	0.28	0.12	0.19	0.18	0.09	0.21
MgO	13.95	14.89	14.16	16.98	14.34	14.96	16.07	14.57	14.54	17.14	14.5	14.78	15.27	14.84
CaO	21.21	21.72	21.31	21.99	21.26	20.17	21.68	21.67	21.87	23.43	22.34	22.11	22.73	22.21
Na2O	0.35	0.31	0.24	0.23	0.3	0.35	0.3	0.22	0.3	0.22	0.23	0.32	0.2	0.32
tot	100.13	98.29	100.51	100.48	100.24	100.94	99.81	100.27	100.14	100.99	101.82	101.87	100.05	100.7
Chemical formula														
Si	1.872	1.914	1.871	1.918	1.858	1.868	1.857	1.858	1.873	1.906	1.852	1.875	1.83	1.836
Al	0.128	0.086	0.129	0.082	0.142	0.132	0.143	0.142	0.127	0.094	0.148	0.125	0.17	0.164
Mg	0.774	0.831	0.781	0.921	0.792	0.822	0.879	0.804	0.804	0.923	0.789	0.803	0.835	0.815
Fe2	0.22	0.184	0.232	0.119	0.201	0.207	0.095	0.186	0.17	0.048	0.183	0.188	0.09	0.115
Fe3	0.062	0	0.034	0.032	0.064	0.098	0.073	0.062	0.083	0.057	0.069	0.059	0.065	0.123
Al	0.039	0.064	0.058	0.035	0.04	0.02	0.057	0.04	0.017	0.018	0.027	0.029	0.072	0.013
Ti	0.026	0.022	0.026	0.014	0.03	0.019	0.015	0.027	0.024	0.007	0.033	0.029	0.02	0.024
Cr	0	0	0.003	0.003	0.001	0	0.004	0.001	0.001	0.021	0.001	0.001	0.007	0.003
Mn	0.008	0.006	0.005	0.003	0.006	0.012	0.002	0.005	0.009	0.004	0.006	0.006	0.003	0.006
Ca	0.845	0.871	0.844	0.857	0.844	0.797	0.852	0.859	0.869	0.907	0.874	0.863	0.893	0.876
Na	0.025	0.022	0.017	0.016	0.022	0.025	0.021	0.016	0.022	0.015	0.016	0.023	0.014	0.023
Classification														
Fs	15.21	10.02	14.31	8.00	14.19	16.34	8.96	13.23	13.55	5.63	13.45	13.18	8.36	12.65
Wo	44.28	46.05	44.53	44.35	44.27	41.17	44.82	44.83	44.91	46.77	45.48	44.98	47.37	45.27
En	40.52	43.93	41.17	47.65	41.54	42.49	46.22	41.94	41.54	47.60	41.07	41.84	44.27	42.08
Mg#	72.7	81.4	74.2	85.7	74.5	72.2	83.8	76.1	75.4	89.4	75.4	76.0	84.1	77.0
GAIA geoTP														
P kbar	1	4.5	1.7	2.6	1.2	1.5	3.1	1.5	1.5	3.5	1.5	0.9	1.3	2.5
1sd	0.4	0.7	0.7	0.4	0.3	0.3	0.6	0.5	0.4	1.2	0.3	0.3	0.5	0.5
T °C	1109	1091	1089	1039	1087	998	1084	1057	1077	1156	1097	1095	1059	1070
1sd	13	9	22	37	17	19	12	10	15	56	15	19	15	14

Table 1 - continued

Eruption	4/3	4/3	17/1	8/8	01 12	01 12	08 03	08 03	03 07	03 07	03 07	03 07	03 07	03 07
date	2011	2011	2013	2014	2017	2017	2018	2018	2019	2019	2019	2019	2019	2019
Activity	ME	ME	ME	NA	ME	ME	ME	ME	P	P	P	P	P	P
Sample	STR040 311	STR040 311	STR170 113	STR080 814	STR011 217a	STR011 217c	STR080 318b	STR080 318b	STR030 719c1	STR030 719c1	STR030 719e2	STR030 719e2	STR030 719h1	STR030 719m
Lithotype	Scoria+ Pumice	Scoria+ Pumice	Scoria+ Pumice	Scoria	Scoria+ Pumice	Scoria+ Pumice	Pumice	Pumice	Pumice	Pumice	Pumice	Pumice	Pumice	Pumice
Zone	core	rim	im inner	core	rim	core	core	rim	rim	core	core	rim	rim	core
Major Elements														
SiO2	51.01	51.39	53.41	51.05	49.62	50.31	51.94	50.29	50.68	50.76	50.06	49.57	52.22	51.01
TiO2	0.77	0.28	0.2	0.7	1.01	0.69	0.24	0.85	0.66	0.82	0.84	0.68	0.4	0.66
Al2O3	2.92	3.1	1.79	2.76	3.63	3.82	2.28	3.15	5.01	3.06	2.81	5.32	2.86	2.82
Cr2O3	0.03	0.67	0.64	0.03	0.02	0.18	1.08	0.03	0.23	0.02	0.01	0.21	0.08	0.04
Fe2O3	4.52	2.57	-	2.6	2.64	2.57	2.25	3.03	1.07	2.29	2.91	2.25	1.39	2.25
FeO	7.32	1.45	3.5	7.25	5.84	3.98	1.32	5.07	3.8	6.12	8.22	3.05	3.92	7.28
MnO	0.32	0.08	0.11	0.22	0.23	0.13	0.07	0.2	0.11	0.23	0.37	0.13	0.12	0.33
MgO	15.61	16.99	16.99	15.86	14.38	15.42	17.6	15	15.56	14.9	14.75	15.61	16.82	14.91
CaO	18.97	22.78	22.58	18.79	21.25	21.76	22.12	21.24	22.21	21.17	18.65	21.7	21.71	20.03
Na2O	0.4	0.15	0.21	0.4	0.28	0.28	0.25	0.35	0.23	0.3	0.4	0.21	0.2	0.37
tot	101.87	99.46	99.43	99.66	98.9	99.14	99.15	99.21	99.56	99.67	99.02	98.73	99.72	99.7
Chemical formula														
Si	1.868	1.885	1.958	1.898	1.864	1.869	1.907	1.877	1.863	1.888	1.887	1.839	1.914	1.901
Al	0.126	0.115	0.042	0.102	0.136	0.131	0.093	0.123	0.137	0.112	0.113	0.161	0.086	0.099
Mg	0.852	0.929	0.928	0.879	0.805	0.854	0.963	0.835	0.853	0.826	0.829	0.863	0.919	0.829
Fe2	0.224	0.044	0.107	0.225	0.183	0.124	0.041	0.158	0.117	0.19	0.259	0.094	0.12	0.227
Fe3	0.125	0.071	0	0.073	0.075	0.072	0.062	0.085	0.03	0.064	0.083	0.063	0.038	0.063
Al	0	0.02	0.035	0.018	0.025	0.036	0.005	0.015	0.08	0.023	0.012	0.071	0.038	0.025
Ti	0.015	0.008	0.006	0.02	0.029	0.019	0.007	0.024	0.018	0.023	0.024	0.019	0.011	0.018
Cr	0.001	0.019	0.018	0.001	0.001	0.005	0.031	0.001	0.007	0.001	0	0.006	0.002	0.001
Mn	0.01	0.003	0.003	0.007	0.007	0.004	0.002	0.006	0.003	0.007	0.012	0.004	0.004	0.01
Ca	0.744	0.895	0.887	0.748	0.855	0.866	0.87	0.849	0.875	0.844	0.753	0.863	0.852	0.8
Na	0.029	0.011	0.015	0.029	0.02	0.02	0.018	0.026	0.016	0.022	0.029	0.015	0.014	0.027
Classification														
Fs	18.34	6.07	5.75	15.79	13.77	10.40	5.42	12.91	7.98	13.54	18.27	8.55	8.40	15.57
Wo	38.06	46.10	46.05	38.73	44.41	45.11	44.89	43.93	46.59	43.69	38.91	45.71	44.08	41.46
En	43.59	47.84	48.21	45.48	41.82	44.49	49.69	43.16	45.43	42.77	42.82	45.75	47.53	42.96
Mg#	70.4	88.7	89.4	74.2	75.2	81.0	90.2	77.0	85.0	**76.0**	70.1	84.3	85.0	73.4
GAIA geoTP														
P kbar	0.3	3.7	2.9	1.3	1	1.5	3.9	1.5	2.6	**0.9**	0.8	2.9	2.6	1.1
1sd	0.3	0.6	0.4	0.3	0.3	0.3	1.3	0.3	0.5	0.3	0.3	0.5	0.6	0.4
T °C	1123	1174	1089	1111	1089	1033	1198	1060	1046	1059	1002	1062	1046	988
1sd	14	44	9	14	18	8	27	15	18	24	26	12	32	8

Table 2 - Major, trace element, and radiogenic isotope composition of selected samples

Sample	STR8/99j pdf	STR 9/00b pdf	STR 9/00i	STR 10/01c	STR12/02 a0	STR12/02 a0 pdf	STR05040 3t	STR28090 3	STR01090 8	STR06120 8
Date	26/8 1999	6/9/2000	6/9 2000	20/10 2001	28/12 2002	28/12 2002	5/4 2003	28/9 2003	1/9 2008	6/12 2008
Lithotype	Pomice (vetro)	Scoria (vetro)	Pomice (mingl.)	Scoria	Scoria	Scoria (vetro)	Blocco	Scoria	Scoria	Scoria
SiO2	-	-	48.81	49.04	49.31	-	51.24	49.29	50.89	50.72
TiO2	-	-	1.08	1.03	0.99	-	0.88	0.98	0.93	0.93
Al2O3	-	-	16.92	17.88	17.64	-	18.86	17.81	16.89	16.78
Fe2O3	-	-	4.26	2.94	2.90	-	1.19	2.96	-	-
FeO	-	-	5.56	6.28	5.91	-	5.81	5.77	7.77	7.94
MnO	-	-	0.18	0.17	0.17	-	0.14	0.16	0.16	0.16
MgO	-	-	6.28	6.16	6.96	-	6.12	6.83	5.83	6.18
CaO	-	-	11.73	11.16	10.97	-	9.63	11.04	11.33	11.37
Na2O	-	-	2.56	2.54	2.45	-	2.65	2.45	2.54	2.49
K2O	-	-	1.98	2.11	2.10	-	2.83	2.03	2.18	2.12
P2O5	-	-	0.39	0.37	0.37	-	0.58	0.36	0.55	0.54
LOI	-	-	0.26	0.32	0.23	-	0.08	0.31	0.51	0.41
Sum	-	-	100.02	100.00	100.00	-	100.01	99.99	99.59	99.63
Sc	-	-	-	30	32	-	-	30	30	31
V	-	-	282	252	263	-	230	263	271	271
Cr	-	-	46	39	56	-	54	51	30	40
Co	-	-	35	28	33	-	29	33	27	28
Ni	-	-	41	40	42	-	-	35	40	40
Cu	-	-	103	114	95	-	109	102	100	100
Zn	-	-	78	67	72	-	56	72	70	70
Rb	-	-	62	70	61	-	69	62	65	62
Sr	-	-	790	731	781	-	812	798	729	716
Y	-	-	27	24	26	-	26	27	25.4	25
Zr	-	-	149	149	157	-	151	159	185	181
Nb	-	-	18	21	21	-	22	22	22.5	21.4
Cs	-	-	-	-	4.4	-	-	4.7	4.5	4.3
Ba	-	-	886	922	950	-	1149	921	977	950
La	-	-	42	45.1	38.5	-	52	48.1	49.7	47.8
Ce	-	-	99	97.4	82.9	-	97	104.8	91.7	88.7
Pr	-	-	-	-	10.1	-	-	12.5	11	10.7
Nd	-	-	47	44.7	39.0	-	43	46.7	42.2	41.4
Sm	-	-	-	8.56	7.63	-	-	9.07	8.31	8.04
Eu	-	-	-	2.29	2.07	-	-	2.54	2.08	2.05
Gd	-	-	-	-	6.31	-	-	7.74	6.79	6.73
Tb	-	-	-	1.06	0.96	-	-	1.16	0.98	0.97
Dy	-	-	-	-	4.66	-	-	5.81	5.14	5.08
Ho	-	-	-	-	0.88	-	-	1.06	0.98	0.98
Er	-	-	-	-	2.39	-	-	2.85	2.6	2.58
Tm	-	-	-	-	0.322	-	-	0.378	0.377	0.370
Yb	-	-	-	2.35	2.30	-	-	2.61	2.38	2.38
Lu	-	-	-	0.352	0.329	-	-	0.398	0.333	0.329
Hf	-	-	-	3.6	3.4	-	-	3.9	3.7	3.6
Ta	-	-	-	1.4	1.3	-	-	1.5	0.96	0.95
Pb	-	-	24	16	22	-	15	20	18	17
Th	-	-	18	14.3	15.2	-	-	15.9	14.7	14.1
U	-	-	-	3.7	3.7	-	-	3.8	4.2	4.0
87Sr/86Sr	**0.706098**	**0.706205**	**0.706123**	**0.706159**	**0.706151**	**0.706152**	**0.706171**	**0.706154**	**0.706157**	**0.706150**
2se	0.000007	0.000008	0.000006	0.000009	0.000009	0.000006	0.000008	0.000008	0.000006	0.000005
143Nd/144Nd	**-**	**0.512571**	**0.512567**	**-**	**-**	**-**	**-**	**0.512559**	**-**	**-**
2se	-	0.000009	0.000005	-	-	-	-	0.000004	-	-

Table 2 - continued

Sample	STR03050 9s pdf	STR08110 9p1 pdf	STR10011 0b	STR04031 1D pdf	STR17011 3L pdf	STR08081 4L pdf	STR09121 7	STR08031 8a	STR03071 9r	STR03071 9L-WR	STR19072 0 pdf
Date	3/5 2009	8/11 2009	10/1 2010	4/3/2011	17/1 2013	8/8 2014	9/12 2017	8/3 2018	3/7 2019	3/7 2019	19/7 2020
Lithotype	Scoria (vetro)	Pomice (vetro)	Scoria	Scoria (vetro)	Pomice (vetro)	Pomice (vetro)	Scoria	Scoria	Scoria	Pomice	Pomice (vetro)
SiO2	-	-	50.39	-	-	-	50.88	51.22	50.68	49.02	-
TiO2	-	-	0.91	-	-	-	0.95	0.90	0.94	0.90	-
Al2O3	-	-	16.8	-	-	-	17.61	16.72	18.06	17.65	-
Fe2O3	-	-	-	-	-	-	-	-	-	-	-
FeO	-	-	8.14	-	-	-	7.86	7.81	8.06	7.86	-
MnO	-	-	0.16	-	-	-	0.16	0.16	0.16	0.16	-
MgO	-	-	6.11	-	-	-	6.07	5.83	5.88	6.1	-
CaO	-	-	11.74	-	-	-	11.07	11.63	10.92	11.6	-
Na2O	-	-	2.34	-	-	-	2.58	2.42	2.61	2.36	-
K2O	-	-	2.08	-	-	-	2.25	2.17	2.27	1.84	-
P2O5	-	-	0.54	-	-	-	0.55	0.56	0.52	0.49	-
LOI	-	-	0.58	-	-	-	0.49	0.49	0.49	0.62	-
Sum	-	-	99.79	-	-	-	100.47	99.91	100.59	98.60	-
Sc	-	-	31	-	-	-	31	31	31	31	-
V	-	-	263	-	-	-	264	266	282	278	-
Cr	-	-	50	-	-	-	40	40	30	30	-
Co	-	-	31	-	-	-	31	31	32	33	-
Ni	-	-	30	-	-	-	30	40	60	60	-
Cu	-	-	110	-	-	-	110	110	110	120	-
Zn	-	-	60	-	-	-	60	70	70	60	-
Rb	-	-	68	-	-	-	70	72	71	57	-
Sr	-	-	691	-	-	-	746	690	721	675	-
Y	-	-	26.2	-	-	-	26.2	26.6	25.9	23.5	-
Zr	-	-	165	-	-	-	163	158	158	131	-
Nb	-	-	19.9	-	-	-	20.2	20.1	20.7	16.9	-
Cs	-	-	4	-	-	-	4.2	4.3	4.5	3.5	-
Ba	-	-	911	-	-	-	948	934	995	868	-
La	-	-	48.5	-	-	-	48.1	47.6	46	40	-
Ce	-	-	95.4	-	-	-	94.9	95.2	90.9	79	-
Pr	-	-	11	-	-	-	11	10.9	10.8	9.59	-
Nd	-	-	42.8	-	-	-	42.3	42.7	41.2	36.3	-
Sm	-	-	8.46	-	-	-	8.48	8.57	7.92	7.22	-
Eu	-	-	2.2	-	-	-	2.18	2.18	2.14	1.96	-
Gd	-	-	6.72	-	-	-	6.41	6.61	6.92	6.32	-
Tb	-	-	0.92	-	-	-	0.92	0.92	0.98	0.88	-
Dy	-	-	5.11	-	-	-	5	5.05	5.13	4.65	-
Ho	-	-	0.95	-	-	-	0.92	0.96	0.94	0.87	-
Er	-	-	2.66	-	-	-	2.55	2.57	2.62	2.3	-
Tm	-	-	0.37	-	-	-	0.352	0.338	0.353	0.331	-
Yb	-	-	2.22	-	-	-	2.23	2.24	2.24	2.05	-
Lu	-	-	0.33	-	-	-	0.321	0.343	0.342	0.313	-
Hf	-	-	3.4	-	-	-	3.6	3.2	3.5	3.3	-
Ta	-	-	0.93	-	-	-	0.86	0.9	1.15	0.91	-
Pb	-	-	15	-	-	-	15	16	15	13	-
Th	-	-	14.4	-	-	-	14.7	14.5	14.3	11.6	-
U	-	-	3.8	-	-	-	3.8	3.8	4.0	3.0	-
87Sr/86Sr	**0.706171**	**0.706132**	**0.706162**	**0.706204**	**0.706158**	**0.706165**	**0.706188**	**0.706177**	**0.706191**	**0.706229**	**0.706221**
2se	0.000006	0.000006	0.000007	0.000009	0.000006	0.000004	0.000007	0.000007	0.000004	0.000005	0.000006
143Nd/144Nd	**-**	**-**	**0.512566**	**-**	**-**	**-**	**0.512556**	**0.512563**	**0.512555**	**0.512548**	**-**
2se	-	-	0.000006	-	-	-	0.000005	0.000004	0.000005	0.000005	-

Table 4.2.2 Major, trace element and radiogenic isotope composition of selected samples

5. UNIROMA 1

5.1 *Factors controlling the triggering and evolution of different eruptive scenarios for the Quaternary potassic magmatism of central Italy: an experimental petrology study*

Activity goals. Understanding the initiation processes of volcanic eruptions through an experimental study of volatile solubility, phase relationships, and crystallization kinetics in potassic magmas.

Research Objectives. This research addressed experimentally the controlling factors for the triggering and evolution of different eruptive scenarios linked to the Quaternary potassic magmatism of central Italy. It focused on magma differentiation and magma-rock interaction processes during ascent and storage at different depths, which reflect in the pre-eruptive magma properties. Specifically, three lines of experimental research were conducted: i) high and low-pressure experiments on phase relations of magmas, shoshonitic, tephri-phonolitic to phonolitic in composition, under hydrous conditions, to constrain the stability fields of particularly pressure-sensitive mineralogical phases; ii) magma-rock interaction experiments to quantify crustal contamination effects and iii) time-series crystal-melt reaction experiments to define melt-mush kinetics and textures.

Methods. Representative compositions of volcanic products from the Roman and Campanian Provinces were chosen as starting materials for phase-relation and magma-rock and crystal-melt interaction experiments. The experimental strategies (i.e., type of experiments, timing and operating conditions such as pressure, temperature, volatile content and oxygen fugacity) were planned after petrographic and geochemical characterization of natural samples. Experiments were conducted in a ½ inch piston-cylinder apparatus at the HP-HT Laboratory of the Department of Earth Sciences, Sapienza Università di Roma. The experimental samples were characterized texturally and chemically by means of a scanning electron microscope (SEM) and an electron probe microanalyzer (EMPA).

Results. In order to select the most suitable natural compositions to use as starting materials for the experimental investigation, a detailed study of the eruptive products of the Ventotene volcano (Pontian Islands, Tyrrhenian Sea) was conducted. The study provided a complete reconstruction of the stratigraphy and magmatic evolution of the Ventotene volcano, in light of geological field mapping and geochemical-petrological characterization of bulk rocks and glass components [1, 2]. Ventotene volcano was chosen as a case study because, like other Quaternary volcanoes in central Italy, it exhibits a shift from early pure Plinian eruptions to a late caldera-forming event. Results indicate that this transition is fundamentally determined by the depth and geometry of the pre-eruptive magmatic systems (Fig. 5.1.1). In particular, pure Plinian scenarios are driven by polybaric differentiation and/or deep storage in reservoirs with high roof depth/width aspect ratios that prevent mechanical failure. In contrast, caldera-forming eruptions are favored by isobaric differentiation in shallow systems at pressures ≤180 MPa, where low roof aspect ratios facilitate decompression-driven collapse upon initial magma withdrawal (Fig. 5.1.1). Ultimately, the ca. 200 MPa critical pressure threshold provides implications for the monitoring and hazard assessment of restless volcanic systems such as Ischia and Campi Flegrei.

1. Phase-relation experiments

These experiments were designed to reproduce the diverse composition and crystal cargo of natural juvenile pyroclasts from Ventotene volcano. The experiments were conducted under hydrous conditions at high (600 MPa, i.e., analogous to magma emplacement at the base of the crust), medium (300 MPa) and low (150 MPa,

i.e., analogous to pre-eruptive magmatic conditions) pressure, allowing us to constrain the pre-eruptive storage conditions in shoshonitic, tephri-phonolitic, and trachy-phonolitic magmas and, in particular, the stability fields of P-sensitive mineral phases (e.g., primary analcime, a mineral phase present in the trachy-phonolitic pumice clasts from the pure Plinian eruptions). The experimental products across all compositions typically consist of glass coexisting with crystal phases in variable proportions depending on the temperature. Phase stability and the resulting melt chemistry were found to be strongly dependent on pressure (P) and temperature (T) conditions, and water saturation levels.

1.1. Shoshonitic composition (MGT)

Experiments on the MGT shoshonite at H2O-undersaturated conditions were performed to identify liquidus temperatures and the sequence of crystallization at different crustal depths (Table 5.1.1).

- At 600 MPa, the near-liquidus temperature is 1100 °C, where clinopyroxene and magnetite initiate crystallization. As the temperature decreases to 1070 °C, plagioclase joins the mineral assemblage. The residual melt undergoes significant differentiation, transitioning from shoshonitic to trachytic composition at 1020 °C (Fig. 5.1.2a, Fig. 5.1.3).
- At 150 MPa, with near-liquidus temperature of 1075 °C, rare euhedral clinopyroxenes occur along with oxides. At 1025 °C and 1000 °C, the paragenesis consists of clinopyroxene+oxides+olivine+plagioclase. Texturally, the crystals exhibit euhedral to subeuhedral habits. At 1000 °C, the system is highly crystallized, and the residual glass reaches a latitic composition. Olivine appears to be in chemical disequilibrium with the melt (Fig. 5.1.2b, Fig. 5.1.3).

Table 5.1.1. Experimental Phase Relations and Melt Evolution for MGT shoshonite

P (MPa)	T (°C)	Paragenesis	Glass Composition
600	1100	Cpx + Ox	Shoshonite
600	1070	Cpx + Ox + Pl	Latite
600	1020	Cpx + Ox + Pl	Trachyte
150	1075	Cpx + Ox	Shoshonite
150	1025	Cpx + Ox + Ol + Pl	Latite
150	1000	Cpx + Ox + Ol + Pl	Latite

Notes: Cpx: clinopyroxene; Ox: oxides; Pl: plagioclase; Ol: olivine.

1.2. Tephri-phonolitic composition (MD1)

The MD1 experiments highlight the influence of water saturation and thermal history on mineral stability, particularly for plagioclase and olivine.

- At 600 MPa and H2O-undersaturated conditions, residual glasses are generally poorly vesicular and crystals are euhedral or sub-euhedral. Clinopyroxene is present in all these experiments as the most abundant mineral phase; it frequently hosts melt inclusions. At 1050 °C, clinopyroxene is the sole liquidus phase. At 950 and 840 °C, the assemblage comprises clinopyroxene, plagioclase, biotite, oxides, and apatite. Rare olivine relicts are observed, often surrounded by biotite microcrysts, suggesting a peritectic reaction. Replicate experiments using a double-step heating strategies confirm that olivine does not constitute an equilibrium phase under the investigated conditions.

- At 600 MPa and H2O-oversaturated conditions, the degree of crystallization is quite low (< 5-15 vol%). At 950 °C, the paragenesis consists of biotite, clinopyroxene, apatite, plagioclase, and magnetite. Double-step heating strategies at 900-950 °C successfully stabilized plagioclase and eliminated metastable olivine, which was otherwise present in single-step heating runs. To note the occurrence of amphibole and very rare albite grains at 840 °C. The residual glasses in these high-pressure runs vary from phonolite to trachyte (Fig. 5.1.2c, Fig. 5.1.3).

- At 300 MPa and H2O-oversaturated conditions, the experimental products show a very low degree of crystallization (< 5 vol%). The paragenesis consists of biotite and clinopyroxene at 950 °C, to which magnetite is added at 900 °C (Fig. 5.1.2d, Fig. 5.1.3).

Table 5.1.2. Experimental Phase Relations for MD1 tephri-phonolite

P (MPa)	H2O conditions	T (°C)	Paragenesis	Glass Composition
600	Undersaturated	1050	Cpx	Phonolite
600	Undersaturated	900	Cpx+Pl+Bt+Ox+Ap	Phonolite
600	Undersaturated	840	Cpx+Pl+Bt+Ox+Ap	Trachyte
600	Oversaturated	950	Cpx+Bt +Ap+Ox+Pl	Phonolite
600	Oversaturated	900	Cpx+Bt +Ap+Ox+Pl	Phonolite
600	Oversaturated	840	Cpx+Bt+Ap+Ox+Pl+Amph	Trachyte
300	Oversaturated	1000	Cpx	Phonolite
300	Oversaturated	950	Cpx+Bt+Ox	Trachy-phonolite
300	Oversaturated	900	Cpx+Bt+Ox	Trachy-phonolite

Notes: Bt: biotite; Ap: apatite; Amph: amphibole; others as above.

1.3. Trachy-phonolitic composition (UCB2)

The UCB2 experiments were performed under H2O-oversaturated conditions.to delineate the pressure-dependent stability of hydrous feldspathoids, which can be used as indicators of deep-seated magma differentiation.

- At 600 MPa and 900 °C, the paragenesis is characterized by euhedral hydrous (Na-K)-feldspathoid with a distinctive hexagonal habit and sizes up to 20 μm, alongside plagioclase and oxides. Biotite joins at 850 °C, and K-feldspar appears at 750 °C. At 750 °C the system is strongly crystallized and lacks hydrous (Na-K)-feldspathoids. As temperature decreases to 700 °C, the abundance of K-feldspar increases, while plagioclase decreases. The residual glass differentiates from trachyte (850-900 °C) to rhyolite (700-750 °C; Fig. 5.1.2e, Fig. 5.1.3).

- At 150 MPa, the experimental products consist of highly vesicular glass coexisting with K-feldspar, plagioclase, and oxides. Notably, hydrous feldspathoids are absent, and K-feldspar is the dominant mineral phase. The residual glass is rhyolitic (Fig. 5.1.2f, Fig. 3).

Table 5.1.3. Experimental Phase Relations and Melt Evolution for UCB2 trachy-phonolite.

P (MPa)	T (°C)	Paragenesis	Glass Composition
600	900	Hyd-Fsp + Pl + Ox	Trachyte
600	850	Hyd-Fsp + Pl + Ox + Bt	Trachyte
600	750	Kfs + Bt + Pl + Ox	Rhyolite
600	700	Kfs + Bt + Pl + Ox	Rhyolite
150	800	Kfs + Pl + Ox	Rhyolite
150	750	Kfs + Pl + Ox	Rhyolite

Notes: Hyd-Fsp: hydrous feldspathoid; Kfs: K-feldspar; others as above.

Phase-equilibrium experiments carried out so far, indicate that Na-K hydrous feldspatoids are only able to crystallize from H2O-saturated trachy-phonolitic (UCB2) magmas at P > 150 MPa. This confirms that pressure (depth) is the primary controlling factor on the differentiation path of these alkaline systems. Moreover, experimental results support the hypothesis that pure Plinian activity is favored by deep, polybaric magma differentiation, whereas isobaric differentiation in shallow, sill-like chambers may lead to underpressure caldera-forming events [1].

2. Open system melt-rock interaction experiments

The experiments performed at 800 MPa, under equilibrium and thermal-gradient conditions, provided the first experimental constraints on the contamination of peri-Tyrrhenian, mantle-derived, K-basaltic magmas during ascent by interaction with a restitic crust of the Hercynian basement. In particular, open-system experiments were designed to simulate the interaction between mantle-derived primitive K-basaltic magma and the lower continental crust, represented by a leucosome-depleted migmatite. These experiments were performed at a pressure of 800 MPa, corresponding to the crust-mantle boundary, within a temperature range of 1050 °C to 1250 °C. The research utilized two primary experimental configurations: isothermal (constant T) runs and thermal gradient (T-gradient) runs (Fig. 5.1.4a).

2.1. Isothermal Open-System Experiments

Isothermal experiments investigated the Assimilation-Fractional Crystallization (AFC) process at temperatures exceeding the K-basalt solidus. Results demonstrated that the degree of migmatite assimilation and the resulting melt chemistry are highly temperature-dependent.

- At 1200 °C, the migmatite is completely melted. Runs with shorter dwell times (1 h) showed significant modal and compositional heterogeneity of the hybrid residual glass, while longer runs (2 h) produced a more homogeneous hybrid glass of K-trachybasaltic composition. The absence of plagioclase in the 2 h run suggests that the assimilation of H2O- and K2O-rich migmatite lowered the liquidus temperature of the system.
- At 1150 °C and 1125 °C, the migmatite was almost fully melted but retained its original shape, acting as a rheological barrier. Evidence of mingling and mixing was observed at the contact zone between the K-basaltic and migmatitic melts. The residual glass compositions shifted from shoshonite in the basaltic zone toward trachyte near the migmatitic zone (Fig. 5.1.4b).

Table 5.1.4: Characteristics of Zones in Isothermal Experiments

Run	Capsule Zone	Description	T (°C)	Time (hour)	Crystallization Degree (vol%)	Phase Assemblage
APR16_M2	Top	Moderate crystalline	1200	1	~27	Gl + Cpx + Ol + Ox
	Bottom	Moderate-High crystalline			~49	Gl + Cpx + Pl + Ol + Ox
APR16_M4		Moderate crystalline	1200	2	~25	Gl + Cpx + Ol + Ox
APR16_M3	Basaltic	High crystalline	1150	1	~53	Gl + Cpx + Pl + Ol + Ox
APR16_M5	Basaltic	High crystalline	1140 - 1000	1	~59	Gl + Cpx + Pl + Ol + Ox

Note: Gl = glass; Cpx = clinopyroxene; Pl = plagioclase; Ol = olivine; Ox = oxide

2.2. Thermal Gradient Experiments

The T-gradient experiments (hot spot at 1250 °C) were specifically designed to prevent the total melting of the crustal rock while simulating the AFC process across a wide range of temperatures. This setup revealed five distinct zones characterized by varying degrees of crystallization and specific phase assemblages (Fig. 5.1.4a).

Table 5.1.5: Characteristics of Zones in Thermal Gradient Experiments

Zone	Description	T Range (°C)	Crystallization Degree (vol%)	Phase Assemblage
1	Moderate crystalline	1250 - 1210	~35	Gl + Cpx + Pl + Ol + Ox
2	Moderate-High crystalline	1210 - 1180	~40	Gl + Cpx + Pl + Ol + Ox
3	High crystalline	1180 - 1160	~55	Gl + Cpx + Pl + Ol + Ox
4	High crystalline	1160 - 1140	~60	Gl + Cpx + Pl + Ol + Ox
5	Holocrystalline	1140 - 1000	100	Pl + Cpx + Ol + Ox

Note: Gl = glass; Cpx = clinopyroxene; Pl = plagioclase; Ol = olivine; Ox = oxide

Open-system isothermal experiments evidence that trachybasaltic to shoshonitic melts (Fig. 5.1.4b), obtained in the experimental AFC process, form a differentiation trend characterized by a positive correlation between Al_2O_3 and SiO_2 (Fig. 5.1.4c), even when plagioclase begins to crystallize, and by a higher silica/alkali ratio compared to closed system experiments conducted at equilibrium conditions using a primitive K-basalt as starting material. In addition to the AFC process, open system experiments at 1150 and 1125 °C show evidence of a concomitant mixing process that originates more evolved latitic melts. The texture of the T-gradient experimental products confirms that, even in this case, the AFC process is well simulated. However, the K_2O and SiO_2 contents of residual glasses, shoshonitic to phono-tephritic in composition, highlight differences with respect to the isothermal experimental trend. Indeed, low temperature zones of the T-gradient experiments exhibit glasses with the highest alkali content, whereas the silica content remains almost constant. These differences can be essentially attributed to the biotite breakdown during the assimilation of migmatite, leading to an increase in Al, Mg, Fe, Ti, and K activities and a decrease of Si activity in the system. The shoshonitic composition obtained from the T-gradient experiments might reproduce the parental magma for the differentiated rock types of Campi Flegrei and Vesuvius (Fig. 5.1.4b,c). On these grounds, near-primary, K-basaltic magmas would be modified within the lower crust,

where they mix with partially melted Hercynian basement rocks. During this process, these magmas differentiate towards shoshonitic-latitic compositions and eventually evolve at shallow depths by interaction either with feldspar-rich crystal mush zones beneath Campi Flegrei or with Meso- Cenozoic limestone and dolostone substrate of Vesuvius (Fig. 5.1.5 a,b) [3].

3. Time-series melt-crystal reaction experiments

These experiments were carried out on a Campi Flegrei K-basaltic starting material and diopsidic clinopyroxenes (CpxL) in chemical disequilibrium with the reacting melt. Experimental details are in Table 5.1.6.

Table 5.1.6. Experimental Parameters and System Configuration

Parameter	Value/Description	Strategic Significance
Pressure	600 MPa	Accurately replicates mid-lower crustal storage depths (approx. 20-22 km).
Temperature	1300 °C	Set ~30 °C above the APR16 liquidus to drive controlled super-liquidus dissolution.
Starting Materials	APR16 K-basalt / Diopsidic Clinopyroxene (Wo48-En46-Fs6)	Models the interaction between primitive mantle-derived recharge and existing cumulate minerals.
Experimental Duration	15, 30, and 90 minutes	Captures the transition from transient dissolution to steady-state recrystallization.
Crystal Geometry	1x1x2 mm parallelepiped monocrystal	Provides a known surface area to volume ratio for kinetic modeling.
Orientation	c-axis perpendicular to capsule bottom	Standardizes the reactive interface; monitored via Pt-wire welding to ensure textural integrity.
Phase Ratio	Powder/Crystal weight ratio of ~3	Ensures a melt-dominated system to facilitate observable geochemical flux and diffusion.

Experimental results (Fig. 5.1.6a,b,c), summarized in Table 5.1.7, show that CpxL crystals dissolve in the first 15 min of the experiment. Clinopyroxene displays rounded crystal edges and sharp crystal-glass interface. In places, glass-filled channels and/or small pores are observed in crystal cracks or cleavages. Experimental glass composition is basaltic (Fig. 5.1.6d), although the higher CaO and MgO contents than in the starting K-basalt reflect the partial dissolution of CpxL. By increasing the experimental dwell time to 30 min, clinopyroxene exhibits both dissolution and recrystallization features marked by the overgrowth of a thin (~10-15 mm) rim on the smoothed edges of the pristine crystal. In the 30-90 min isothermal rest-time experiments, a population of euhedral, zoned, <15 mm clinopyroxene microcrysts surround the initial crystal. In these latter experiments, the composition of the residual glasses varies from K-basalt to trachybasalt, to shoshonite (Fig. 5.1.6d). These experimental findings indicate that minor thermal fluctuations of ~30 °C can induce rapid re-equilibration, suggesting that clinopyroxene-rich mush zones beneath volcanic systems like Campi Flegrei can be effectively unlocked and mobilized by injections of primitive magma.

Table 5.1.7. Temporal Evolution of Textures and Melt Chemistry

Dwell Time (min)	Predominant Process	Textural Observations	Glass Compositional Trend
15	Dissolution	Rounded edges; glass-filled channels/pores	Basaltic: increase of CaO and MgO contents
30	Dissolution & Recrystallization	10–15 µm overgrowth rims on smoothed edges	Transition toward trachybasalt
90	Dissolution & Extensive Recrystallization	Euhedral, zoned new microcrysts (<15 µm)	Shoshonitic: Low CaO/MgO; High Al2O3 and alkalis

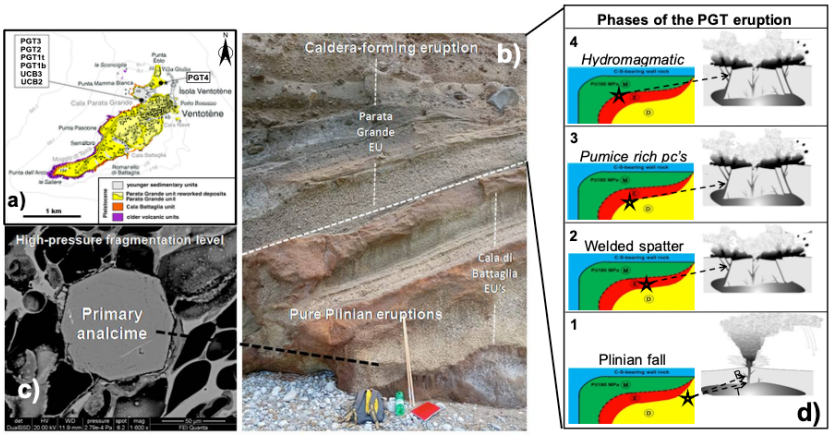

Figure 5.1.1. Sketch map (a) and close-up of a volcanic outcrop at Ventotene (b); (c) Back-scattered electron (BSE) images of Plinian pumice clasts from the Cala Battaglia unit, showing euhedral analcime microlites surrounded by abundant vesicles. (d) Sketch showing the feeder magma zones involved in the different phases (1-2-3-4 through time) of the PGT caldera forming eruption (modified after Gaeta et al., 2025).

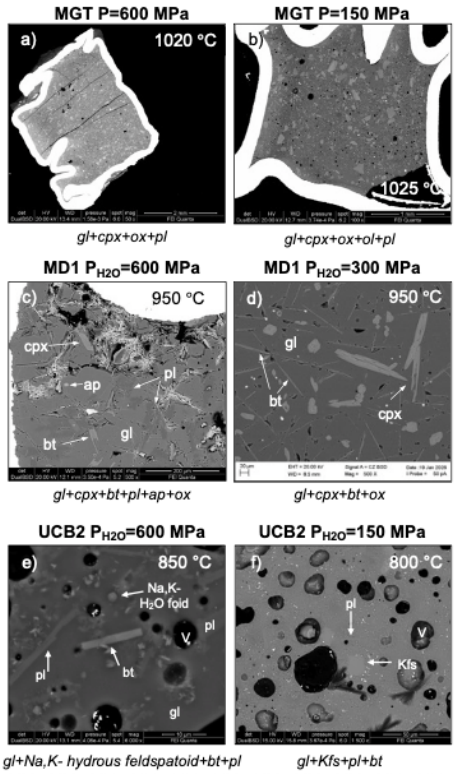

Figure 5.1.2. Back-scattered electron (BSE) images of the experimental products (a,b) shoshonite (MGT) (c,d) tephri-phonolite (MD1) and (d, e) trachy-phonolite (UCB2) starting materials. ap = apatite; bt = biotite; cpx = clinopyroxene; gl = glass; K-feld = K-feldspar; pl = plagioclase; ol = olivine; ox = oxide; V=vesicle.

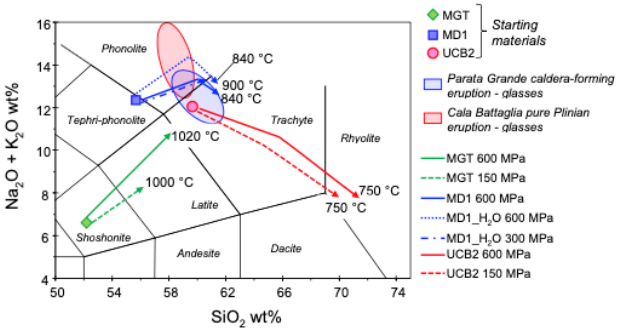

Figure 5.1.3. Variation in composition of experimental residual glasses plotted in the Total alkali (Na2O + K2O) vs silica (SiO2) classification diagram (TAS; Le Maitre, 2002) starting from a shoshonite (MGT), tephri-phonolite (MD1) and a trachy-phonolite (UCB2).

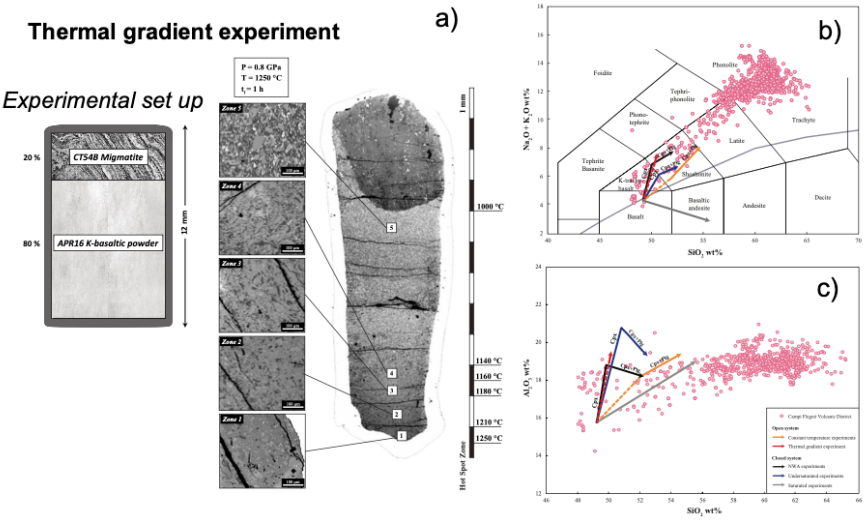

Figure 5.1.4. Scheme of the starting configuration and final product of the thermal-gradient experiment (a). Variation in composition of residual glasses produced by experiments isothermal and T-gradient experiments plotted in the TAS classification diagram (b) and in the SiO2 vs Al2O3 diagram (c).

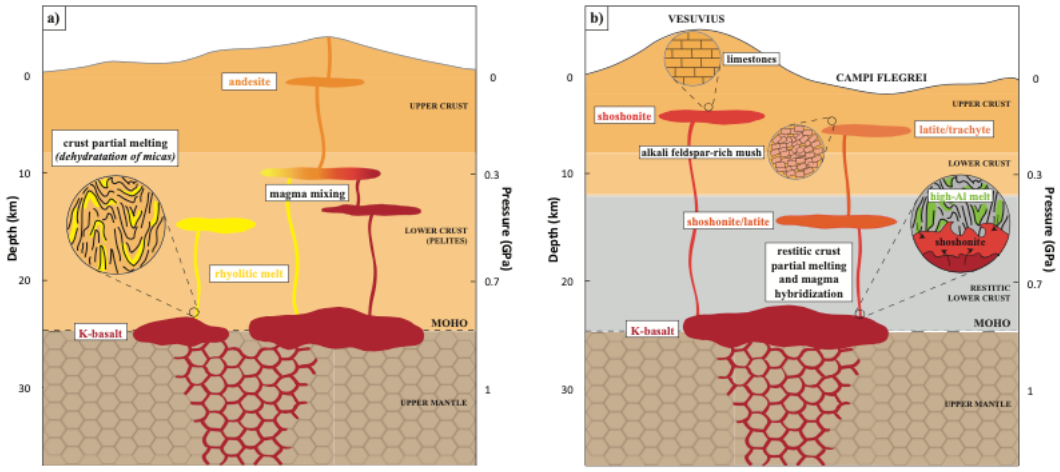

Figure 5.1.5. Sketch models of (a) lower crust partial melting dominated by anatectic Si-rich melts associated to an early calc-alkaline volcanic cycle and (b) assimilation of a restitic lower crust (Hercynian basement) dominated by high-Al melts, resulting into the differentiation of primitive K-basalt magmas toward a shoshonitic composition. This scenario may explain the origin of common parental magmas at Campi Flegrei and Vesuvius, which then depart compositionally due to shallow interaction with alkali feldspar-rich rock/mush and with Meso-Cenozoic limestone/dolostone wall rocks, respectively.

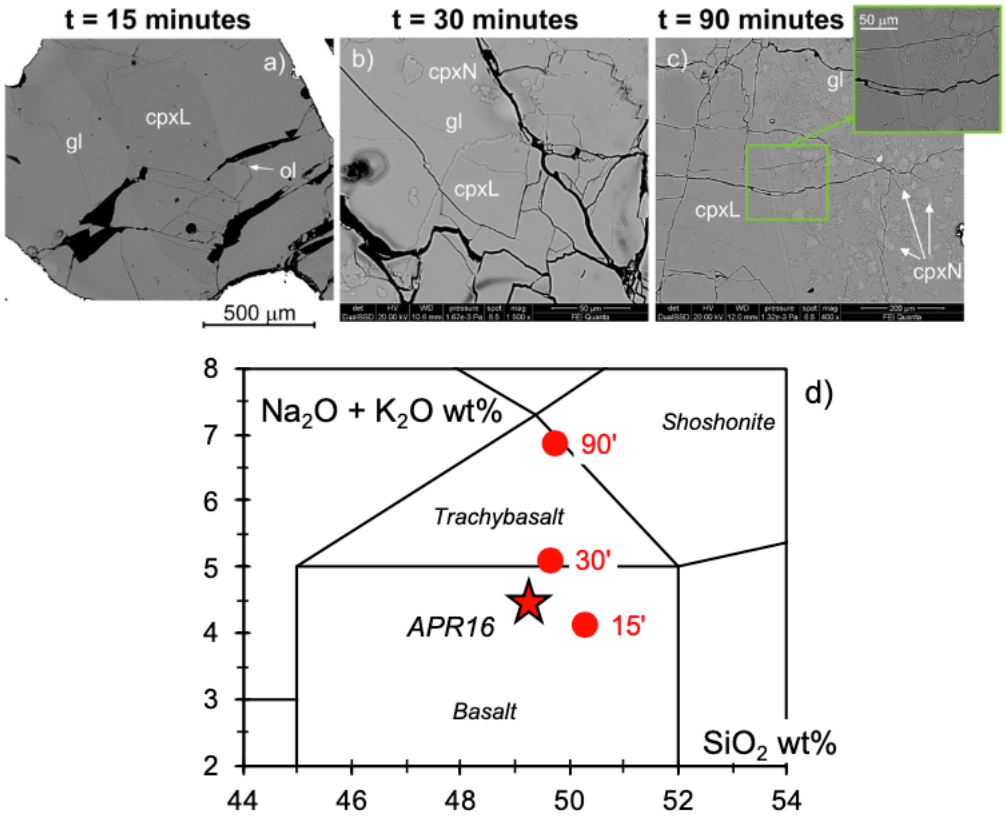

Figure 5.1.6. BSE images of experimental charges from time-series cpx-K basalt reaction experiments showing (a) dissolution features of the starting cpx (cpxL), i.e., rounded crystal edges, glass-filled channels and/or small pores; longer runs (b, c) show the overgrowth of a thin (~10-15 mm) rim on the smoothed cpxL crystal edges, as well as the crystallization of new, euhedral, zoned cpx (cpxN). Variation of composition of experimental residual glasses plotted in the TAS classification diagram (b) gl=glass; ol= olivine.

6. UNINA

6.1 *Factors controlling the triggering and evolution of different eruptive scenarios for the Quaternary potassic magmatism of central Italy: an experimental petrology study*

Activity goals. The current episode of volcanic unrest at Campi Flegrei caldera, which began in 2005, and the advent of a localized geodetic anomaly in 2021 underscore the urgency of improving our understanding of the processes governing eruptive behavior, particularly transitions between explosive and effusive activities, to refine volcanic hazard/risk assessments and upgrade emergency planning. Therefore, stratigraphy, geochemistry and petrology of the 4.3-ka Accademia explosive-effusive volcanic deposits were studied to understand the conditions and processes of phase transition in Campi Flegrei eruptions and shed light on the link between magma ascent and the ongoing unrest episode.

Main results achieved. Stratigraphically, on the southern side, volcanic deposits of Accademia eruption lie on marine sediments and below the eruptive deposits of Solfatara and Astroni eruptions, respectively. Four distinct units, A to D from base to top, were observed in the eruptive sequence of this eruption (Fig. 1): (1) unit A is composed of light brownish massive ash layers with coarser clasts of mainly scoria lapilli and subordinately scoria bomb (*i.e.* massive scoria lapilli ash (mscLT); thickness > 0.8 m); (2) unit B refers to dark grayish massive scoria bomb layers with finer clasts of dominantly scoria lapilli and subordinately ash (*i.e.* massive scoria agglomerate (mscAg); thickness >1.5 m).; (3) unit C is a layer of reddish mscAg with a thickness above 3 m.; and (4) unit D refers to the light grayish massive lava with a maximum outcropping thickness of ~65 m. Textural investigations revealed a porosity above 50% for the explosive deposits and below 20% for the effusive deposits. In addition, the matrix is glassy in units A and C and crystalline in units B and D (Fig. 6.1.1). The deposits showed a trachytic composition (59.47–60.05 wt.% SiO_2 and 11.62–12.81 wt.% Na_2O+K_2O on a water-free basis; Fig. 6.1.2a and Table 6.1.1) with an estimated 3 wt.% of water content (uncertainty: ~0.7 wt.%; Fig. 6.1.2c). Optical and electron microscopy indicated that feldspar and clinopyroxene are the main phenocrysts in a groundmass of mostly sanidine microlites (Fig. 6.1.1).

Our petrological studies indicate: (1) the presence of antecrysts, such as Ca-rich plagioclase and Mg-rich clinopyroxene, that are not in equilibrium with the host trachytic magma erupted, but with less-evolved trachitic and latitic magmas; (2) reverse and oscillatory zoning in clinopyroxene phenocrysts; (3) the frequent clinopyroxene crystals with resorbed rims in the groundmass of the effusive deposits; and (4) a decrease in orthoclase content from core to rim in sanidine phenocrysts, revealing reheating of the magma prior to eruption (Arzilli et al., 2020). These observations demonstrate destabilization of the magmatic system by the intrusion of less-evolved magma batches from a depth of 8–10 km (200–250 MPa; Fig. 6.1.2b) into a shallower trachytic reservoir at a depth of 6–8 km (150–200 MPa; Fig. 2b). The Sr and Nd isotope studies of Arienzo et al. (2016) showed that the magma feeding Accademia eruption originated from mixing/mingling of two end-members compositionally similar to NYT and Minopoli 2 magmas. The latter represents the most primitive end-member erupted in Campi Flegrei volcanic history (Smith et al., 2011).

Following eruption triggering, the magma with pre-eruptive temperatures of 950–980 °C (Fig. 6.1.2b) ascended rapidly (on the order of hours to 1–2 days, as constrained by phlogopite stability; Fabbrizio and Carroll, 2008) through feeder-dyke structures along the major pre-existing volcano-tectonic features (Fig. 6.1.3a), interacted with external water (*i.e.* seawater and/or groundwater), and generated a phreatomagmatic eruption responsible for unit A emplacement. The stability of sodalite indicates that the

trachytic magma subsequently stalled or slowly ascended at a depth of ~2 km (40–50 MPa; Arzilli et al., 2016), where sanidine crystallized within the groundmass, overpressure increased, and a purely magmatic eruption led to the emplacement of unit B. Phreatomagmatic and magmatic explosive activities repeatedly alternated, resulting in the deposition of units A to C with an overall thickness of about 15 m (Fig. 6.1.3b). The ascent velocity of the degassed to partially degassed magma with pre-eruptive temperatures above 980 °C (Fig. 6.1.2b) decreased again at ~2 km depth, promoting extensive sanidine crystallization in the groundmass and ultimately extrusion of approximately 10 Mm^3 lava (unit D) without encountering external water (Fig. 6.1.3c). The effusive activity formed a trachytic lava dome with an estimated maximum thickness of 120 m on the explosive deposits, which turned into a thick lava flow southward.

The results show that volcano-tectonic faults played a pivotal role in magma ascent following eruption triggering and in effusion of the highly crystalline magma. Volcanic hazards related to lava effusion could be noticeable in the immediate surroundings of the eruptive vent and national emergency plans need to deal with both explosive and effusive phases of even a small-sized eruption for mitigation measures.

Following the triggering of Accademia eruption, the trachytic magma ascended in hours to 1–2 days from the destabilized reservoir at a depth of 6–8 km and resulted in the phreatomagmatic phase of the volcanic activity. The magma then stalled or slowly ascended at a depth of ~2 km and fed a pure magmatic activity. A shift between the phreatomagmatic and magmatic explosive eruptions occurred multiple times until the degassed to partially degassed lava was effusively extruded. The erupted deposits are mainly emplaced by the effusive phase of Accademia eruption, which highlights that both effusive and explosive phases of even a small-sized volcanic event at Campi Flegrei need to be carefully considered in emergency plans for the current unrest.

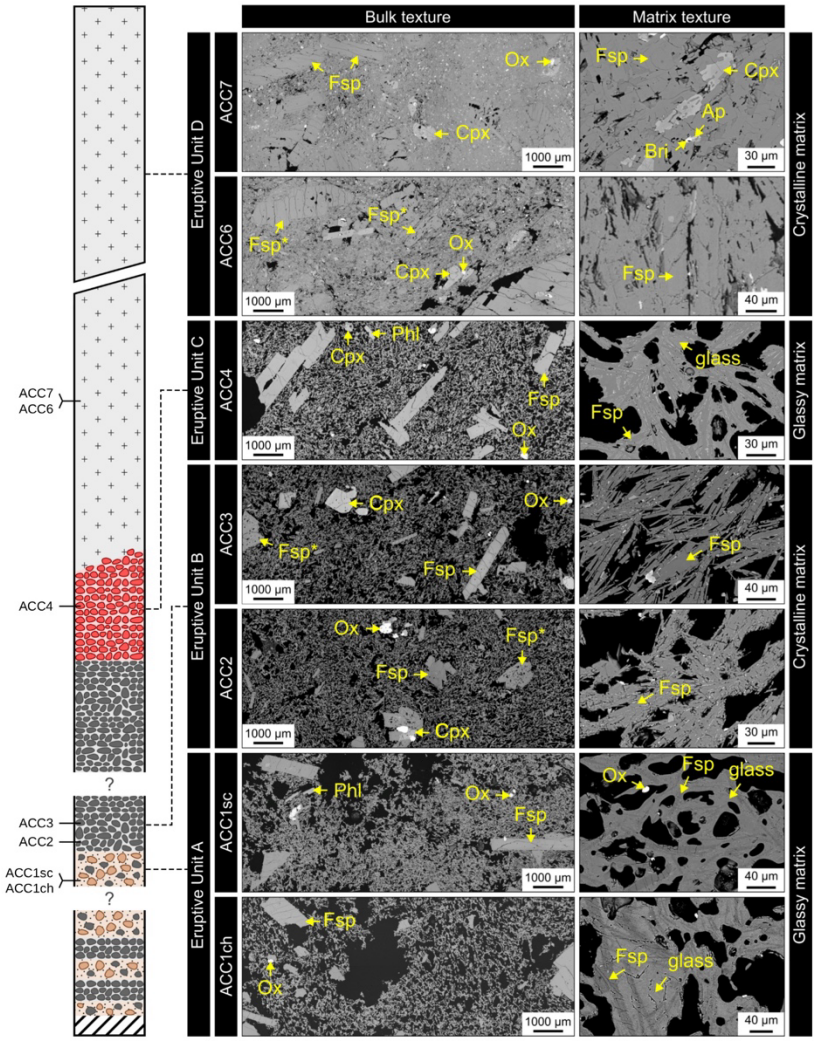

Fig. 6.1.1 SEM images showing bulk and groundmass texture of the scoriae and lavas emplaced by Accademia eruption. Fsp: feldspar; Fsp*: feldspar with sieved texture; Cpx: clinopyroxene; Phl: phlogopite; and Ox: Fe-Ti oxide. The area in black represents the vesicles.

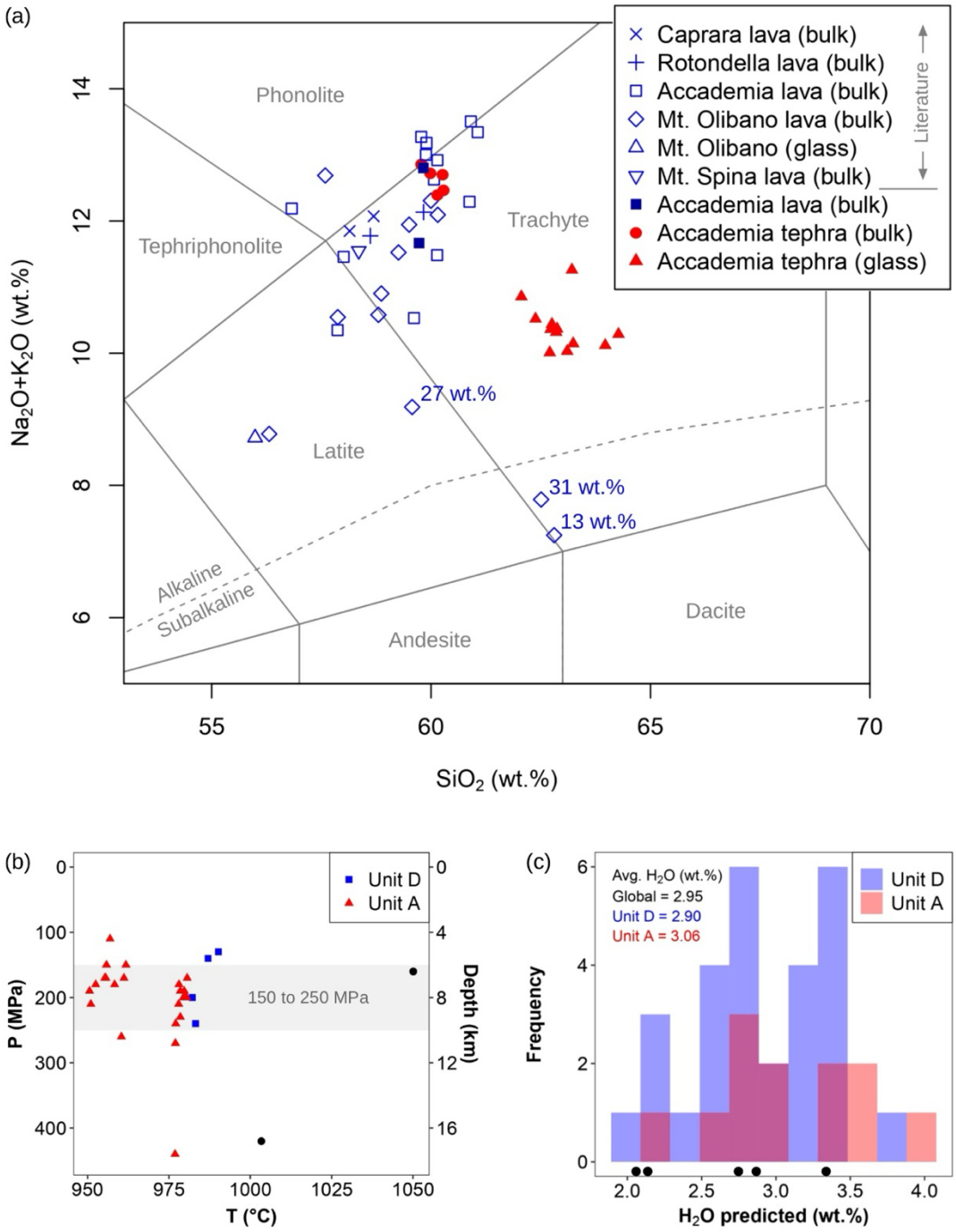

Fig. 6.1.2 (a) Total Alkali vs. Silica classification diagram (TAS; Le Bas et al., 1986) for the post-NYT lava and Accademia scoriae (in blue and red, respectively). The literature data are from Armienti (1981), D'Antonio et al. (1999), Di Filippo et al. (1991), Di Girolamo et al. (1984), Isaia et al. (2009), Mastrolorenzo and Pappalardo (2006), Melluso et al. (2012), Nadeau et al. (2021), Rosi and Sbrana (1987) and Sinno (1955). The values in blue represent the weight loss on ignition.; (b) The estimated temperature and pressure (100 MPa = 4 km) of magma storage in Accademia eruption.; and (c) The predicted H_2O content of the magma feeding Accademia eruption. The black solid symbols refer to the calculations using the mineral chemistry of Accademia lava reported by Melluso et al. (2012).

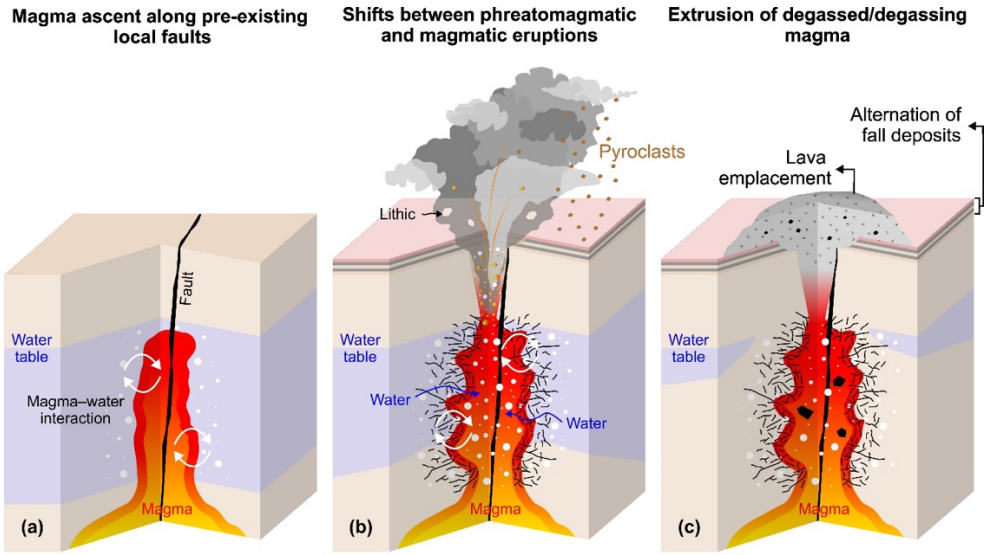

Fig. 6.1.3 Conceptual model of Accademia eruption: (a) Trachytic magma with pre-eruptive temperatures of 950–980 °C and a water content of 3 wt.% preferentially moved through mechanical discontinuities from the destabilized magmatic reservoir at a depth of 6–8 km (150–200 MPa) toward the ground surface with a relatively fast ascent rate and encountered external water; (b) Intensive interaction of magma with water led to magma fragmentation and pyroclast dispersion (unit A) through a phreatomagmatic activity. The magma then stalled or slowly ascended at a depth of ~2 km (40–50 MPa), sanidine crystallized in the groundmass and the increased overpressure resulted in a pure magmatic eruption and emplacement of unit B. The phreatomagmatic and magmatic activities were repeated multiple times and generated several scoria layers (units A to C); and (c) The degassed to partially degassed magma with pre-eruptive temperatures above 980 °C and a water content of 3 wt.% stalled or slowly ascended at the shallow part of the conduit (~2 km; 40–50 MPa) again and promoted groundmass sanidine crystallization. The magma reached the ground surface without interaction with external water and effusively emplaced unit D on the pyroclastic deposits. The angular black symbols represent the mafic xenoliths.

Unit	Sample	SiO_2	TiO_2	Al_2O_3	Fe_2O_3	MnO	MgO	CaO	Na_2O	K_2O	P_2O_5	Loss at 110 °C	Loss at 1000 °C	Total
D	ACC7	59.30	0.46	19.18	3.99	0.13	0.77	2.87	4.09	8.60	0.13	0.11	0.24	99.89
D	ACC6	59.34	0.49	18.84	4.32	0.14	1.25	3.63	3.48	8.11	0.18	0.35	0.74	100.87
C	ACC4	58.47	0.44	18.57	3.89	0.13	0.72	2.73	3.82	8.50	0.13	0.20	0.57	98.17
B	ACC3	60.51	0.48	19.32	4.19	0.15	0.81	2.97	4.50	7.97	0.13	0.19	0.50	101.72
B	ACC2	59.55	0.46	19.01	4.02	0.14	0.78	2.97	4.14	8.49	0.12	0.27	0.46	100.41
A	ACC1ch	58.07	0.45	18.63	3.98	0.14	0.75	2.90	4.14	8.35	0.12	0.36	1.98	99.87
A	ACC1sc	59.57	0.45	19.03	3.95	0.14	0.76	2.86	3.68	8.64	0.12	0.28	0.19	99.67
Recalculated anhydrous														
Unit	**Sample**	**SiO_2**	**TiO_2**	**Al_2O_3**	**Fe_2O_3**	**MnO**	**MgO**	**CaO**	**Na_2O**	**K_2O**	**P_2O_5**			**Total**
D	ACC7	59.59	0.46	19.27	4.01	0.13	0.77	2.89	4.11	8.64	0.13			100
D	ACC6	59.47	0.49	18.88	4.33	0.14	1.25	3.64	3.49	8.13	0.18			100
C	ACC4	60.03	0.45	19.07	4.00	0.13	0.74	2.80	3.92	8.73	0.13			100
B	ACC3	59.89	0.48	19.12	4.15	0.15	0.80	2.94	4.45	7.89	0.13			100
B	ACC2	59.74	0.46	19.07	4.03	0.14	0.78	2.98	4.16	8.52	0.12			100
A	ACC1ch	59.54	0.46	19.10	4.08	0.15	0.77	2.97	4.25	8.56	0.12			100
A	ACC1sc	60.05	0.46	19.18	3.98	0.14	0.77	2.88	3.71	8.71	0.12			100

Table 6.1.1 Bulk rock composition (in wt. %) of the studied deposits determined by Inductively Coupled Plasma-Optical Emission Spectrometry (ICP-OES). A.I.: agpaitic index=(Na+K)/Al on a molecular basis; and Mg#: Mg number=100MgO/(MgO+FeO_t) on a molecular basis.

7. Conclusions

This deliverable presents an integrated reconstruction of the activities performed by three different research units (UNIFI, UNIROMA1 and UNINA) within the framework of WP3.3. The work of the three units concentrated on the "Pre-eruptive physico-chemical magma characteristics" which control explosive eruptions, aimed at the understanding of the main factors responsible of eruptive style and which are the base for a correct assessment of hazards and expected impacts of explosive volcanoes. By combining field-based volcanology, laboratory investigations, geochemical characterization, and experimental petrology the project provides new constraints on the past activity at some of the most hazardous explosive volcanoes in Italy (Vesuvius, Campi Flegrei, Stromboli, Potassic volcanoes of Italy).

Activity at UNIFI concentrated on Vesuvius and Stromboli volcanoes.Stratigraphical, textural, geochemical and petrographical data of the first erupted deposits of Plinian eruptions from Vesuvius allowed to define modalities and timing of pre- and syn-eruptive magma ascent and eruption trigger, and to constrain the expected measurables in case of reactivation. As a general rule, the onset of a large explosive volcanic eruption is generally characterized by a weak transient activity. The products of this opening phase are confined to thin proximal beds of small volume and limited dispersal, and are sometimes difficult to study. The study of the products from the opening phases of the Avellino Plinian eruption of Somma-Vesuvius (Italy) revealed the important role played in the eruption by a magma body present at shallow depth that cooled and partially crystallised under different conditions compared to the main, deeper, and larger magma reservoir feeding the paroxysmal phases of the eruption. Elemental diffusion chronometry suggests that magma movement toward the shallow reservoir anticipated the eruption by a maximum of about 100 years, while the arrival of a last mafic input into the shallow magma body can be confined to only a few years before the eruption. Conversely, the initial phase of the AD79 Pompeii eruption was marked by the early destabilization of the diffusive interface of a compositionally stratified magma reservoir, possibly triggered by the arrival of deep mafic magma batch(es) which only briefly anticipated the eruption. The identification in past activity of Vesuvius of important magma dynamics which preceded some of the most devastating eruptions is basic to suggest the possible path of a volcanic unrest and to interpret data from volcano monitoring.

A large dataset of Sr-Nd isotope ratios on whole rocks and matrix glasses has been collected for the products of different styles of activity of Stromboli volcano. The analysed samples continue and complete the isotopic dataset already available and published, which reported data since the beginning of 1900 CE up to 2007 CE. The new Sr isotopic data evidence important changes since 2007, particularly accentuated in the lp-magma, which suggest variations in the plumbing system dynamics linked to nearly parallel changes in the parental magmas, possibly determined by a heterogeneous and still active mantle source. New collected data on clinopyroxene composition complete a huge dataset, used to yield pressure and temperature estimates using a novel clinopyroxene-only geothermobarometer based on Feedforward Neural Networks (FNN) machine learning technique, so constraining the thermo-barometric conditions of magma ponding in the deep and shallow plumbing system, basilar for the interpretation of present activity and for the assessment of possible future scenarios.

New experimental petrology data were performed at UNIROMA1 on different magma compositions of volcanic products from the Roman and Campanian Provinces were collected to quantitatively address the controlling factors for the triggering and evolution of different eruptive scenarios linked to the Quaternary potassic magmatism of central Italy. Experiments were focused on magma differentiation and magma-rock interaction processes during ascent and storage at different depths, which strongly reflect in the pre-eruptive magma properties. High and low-pressure experiments on phase relations of magmas under hydrous

conditions were used to constrain the stability fields of particularly pressure-sensitive mineralogical phases. Experimental results support the hypothesis that pure Plinian activity is favored by deep, polybaric magma differentiation, whereas isobaric differentiation in shallow, sill-like chambers may lead to underpressure caldera-forming events. Experiments on magma-rock interaction were specifically designed to quantify crustal contamination effects. Results suggest that near-primary, K-basaltic magmas would be modified within the lower crust, where they mix with partially melted basement rocks. During this process, these magmas differentiate towards shoshonitic-latitic compositions and eventually evolve at shallow depths by interaction either with feldspar-rich crystal mush zones (e.g. Campi Flegrei) or, in some cases, with the limestone - dolostone substrate (e.g. Vesuvius). Finally, time-series crystal-melt reaction experiments were performed to define melt-mush kinetics and textures. Experimental findings indicate that minor thermal fluctuations of ~30 °C can induce rapid re-equilibration, suggesting that clinopyroxene-rich mush zones beneath volcanic systems like Campi Flegrei can be effectively unlocked and mobilized by injections of primitive magma.

Researchers from UNINA concentrated on the definition of the magmatic system responsible of the so-called Accademia at Campi Flegrei, pivotal for the present state of the caldera. In fact, the current unrest phase of Campi Flegrei caldera, started on 2005, presented in the last years a deficiency in thee expected uplift anomaly in the area of the Accademia dome, close to Pozzuoli, the center of the maximum present uplifting area. Stratigraphy, geochemistry and petrology of deposits of the 4.3-ka Accademia explosive-effusive eruption were studied just to understand the conditions and processes of eruptive style transition in Campi Flegrei eruptions and to shed light on the link between magma ascent and the ongoing unrest episode. Petrological studies demonstrate the destabilization of a magmatic system at a depth of 6–8 km by the intrusion of less-evolved magma batches from a depth of 8–10 km. Following eruption triggering, the magma ascended rapidly (possibly on the order of hours to 1–2 days through feeder-dykes along the major pre-existing volcano-tectonic features, interacting with external water (i.e. seawater and/or groundwater). The decreased ascent velocity of the degassed to partially degassed magma promoted extensive sanidine crystallization in the groundmass and ultimately extrusion of a trachytic lava dome. The results show that volcano-tectonic faults played a pivotal role in magma ascent following eruption triggering and in effusion of the highly crystalline magma.

6. References

Arienzo, I., Mazzeo, F. C., Moretti, R., Cavallo, A., & D'Antonio, M. (2016). Open-system magma evolution and fluid transfer at Campi Flegrei caldera (Southern Italy) during the past 5 ka as revealed by geochemical and isotopic data: The example of the Nisida eruption. Chemical Geology, 427, 109-124.

Armienti, P. (1981). L'evoluzione della serie potassica dei Campi Flegrei: studio petrologico degli inclusi ignei e delle lave. Atti della Società Toscana di Scienze Naturali, Memorie, Serie A, 88, 83-116.

Arzilli, F., Piochi, M., Mormone, A., Agostini, C., & Carroll, M. R. (2016). Constraining pre-eruptive magma conditions and unrest timescales during the Monte Nuovo eruption (1538 AD; Campi Flegrei, Southern Italy): integrating textural and CSD results from experimental and natural trachy-phonolites. Bulletin of Volcanology, 78(10), 72.

Arzilli, F., Stabile, P., Fabbrizio, A., Landi, P., Scaillet, B., Paris, E., & Carroll, M. R. (2020). Crystallization kinetics of alkali feldspar in peralkaline rhyolitic melts: implications for Pantelleria volcano. Frontiers in Earth Science, 8, 177.

Bragagni A, Avanzinelli R, Freymuth H, Francalanci L (2014) Recycling of crystal mush-derived melts and short magma residence times revealed by U-series disequilibria at Stromboli volcano. Earth Planet Sci Lett 404, 206-219.

Cardello G.L., Aida M. Conte, M. Gaeta, B. Jicha, F. Lombardi, L. Monaco, S. Nomade, C. Perinelli, G. Sottili, D.M. Palladino. Chemostratigraphy and 40Ar-39Ar Geochronology of Ventotene volcano (Pontian Islands, Tyrrhenian Sea), the missing link in the Quaternary potassic magmatism of central Italy. In preparation

Chicchi L, Bindi L, Fanelli D, Tommasini S (2023) Frontiers of thermobarometry: GAIA, a novel deep learning-based tool for volcano plumbing systems. Earth Planet Sci Lett 620, 118352.

Cioni R, Civetta L, Marianelli P, Metrich N, Santacroce R, Sbrana A (1995) Compositional layering and syn-eruptive mixing of a periodically refilled shallow magma chamber: the AD 79 Plinian eruption of Vesuvius. J Petrology

D'Antonio, M., Civetta, L., Orsi, G., Pappalardo, L., Piochi, M., Carandente, A., ... & Isaia, R. (1999). The present state of the magmatic system of the Campi Flegrei caldera based on a reconstruction of its behavior in the past 12 ka. Journal of Volcanology and Geothermal Research, 91(2-4), 247-268.

Di Filippo, G., Lirer, L., Maraffi, S., & Capuano, M. (1991). L'eruzione di Astroni nell'attività recente dei Campi Flegrei. Bollettino della Societa Geologica Italiana, 110(2), 309-331.

Di Girolamo, P., Ghiara, M. R., Lirer, Munno, R., Rolandi, G., & Stanzione, D. (1984). Vulcanologia e petrologia dei Campi Flegreei. Bollettino della Società Geologica Italiana, 103(2), 349-413.

Fabbrizio, A., & Carroll, M. R. (2008). Experimental constraints on the differentiation process and pre-eruptive conditions in the magmatic system of Phlegraean Fields (Naples, Italy). Journal of Volcanology and Geothermal Research, 171(1-2), 88-102.

Francalanci L, Avanzinelli R, Nardini I, Tiepolo M, Davidson JP, Vannucci R (2012) Crystal recycling in the steady-state system of the active Stromboli volcano: a 2.5-ka story inferred from in situ Sr-isotope and trace element data. Contrib Mineral Petrol 163, 109-131.

Francalanci L, Davies GR, Lustenmhower W, Tommasini S, Mason PRD, Conticelli S (2005) Old crystal re-cycle and multiple magma reservoirs in the plumbing system of the present day activity at Stromboli volcano, South Italy: Sr-isotope in situ microanalyses. J Petrol 46, 1997-2021.

Francalanci L, Tommasini S, Conticelli S (2004) The volcanic activity of Stromboli in the 1906-1998 period: mineralogical, geochemical and isotope data relevant to the understanding of Strombolian activity. J Volcanol Geotherm Res 131, 179-211.

Francalanci L, Tommasini S, Conticelli S, Davies GR (1999) Sr isotope evidence for short magma residence time for the 20th century activity at Stromboli volcano, Italy. Earth Planet Sci Lett 167, 61-69.

Gaeta M., C. Perinelli, G.L. Cardello, A.M. Conte, L. Monaco, R. Pavese, G. Sottili, D.M. Palladino, High vs. Low Pressure Magma Chambers at Ventotene Volcano (Tyrrhenian Sea, Central Italy): Implication for Pure Plinian vs. Caldera-forming Eruptions, J. Petrol. 66 (2025) 10.

Isaia, R., Marianelli, P., & Sbrana, A. (2009). Caldera unrest prior to intense volcanism in Campi Flegrei (Italy) at 4.0 ka BP: Implications for caldera dynamics and future eruptive scenarios. Geophysical Research Letters, 36(21).

Landi P, Corsaro RA, Francalanci L, Civetta L, Miraglia R, Pompilio M, Tesoro R (2009) Magma dynamics during the 2007 Stromboli Eruption (Aeolian Islands, Italy): Mineralogical, Geochemical and Isotopic data. J Volcanol Geothermal Res 182, 255-268.

Le Bas, M. J., Le Maitre, R. W., Streckeisen, A., Zanettin, B., & IUGS Subcommission on the Systematics of Igneous Rocks. (1986). A chemical classification of volcanic rocks based on the total alkali-silica diagram. Journal of Petrology, 27(3), 745-750.

Masotta M, Mollo S, Freda C, Gaeta M, Moore G (2013) Clinopyroxene–liquid thermometers and barometers specific to alkaline differentiated magmas. Contrib Mineral Petrol 166:1545–1561. https://doi.org/10.1007/s00410-013-0927-9

Mastrolorenzo, G., & Pappalardo, L. (2006). Magma degassing and crystallization processes during eruptions of high-risk Neapolitan-volcanoes: evidence of common equilibrium rising processes in alkaline magmas. Earth and Planetary Science Letters, 250(1-2), 164-181.

Melluso, L., De'Gennaro, R., Fedele, L., Franciosi, L., & Morra, V. (2012). Evidence of crystallization in residual, Cl–F-rich, agpaitic, trachyphonolitic magmas and primitive Mg-rich basalt–trachyphonolite interaction in the lava domes of the Phlegrean Fields (Italy). Geological Magazine, 149(3), 532-550.

Melluso L, Scarpati C, Zanetti A, Sparice D, de Gennaro R, (2022) The petrogenesis of chemically zoned, phonolitic, Plinian and subPlinian eruptions of Somma-Vesuvius, Italy: role of accessory phase removal, independently filled magma reservoirs with time, and transition from slightly to highly silica undersaturated magmatic series in an ultrapotassic stratovolcano. Lithos 430:106854. https://doi.org/10.1016/j.lithos.2022.106854

Molina JF, Moreno JA, Castro A, Rodríguez C, Fershtater GB (2015) Calcic amphibole thermobarometry in metamorphic and igneous rocks: new calibrations based on plagioclase/amphibole Al-Si partitioning and amphibole/liquid Mg partitioning. Litho

Nadeau, O., Mick, E., Robidoux, P., Grassa, F., Brusca, L., Voinot, A., & Leybourne, M. I. (2021). Lithium isotopes and Cu-Au concentrations in hydrothermal alterations from Solfatara Volcano, Campi Flegrei caldera complex, and La Fossa volcano, Vulcano Island, Italy: Insights into epithermal ore forming environments. Ore Geology Reviews, 130, 103934.

Palummo F., C. Perinelli, B. Bonechi, A. Fabbrizio, V. Misiti, P. Scarlato, M. Gaeta, Experimental Re-melting of a Continental Crust: Probing the Deep Storage Zone of Campi Flegrei and Vesuvius Magmas, Contrib. Mineral. Petrol. 179 (2024) 41.

Petrone CM, Bugatti G, Braschi E, Tommasini S (2016) Pre-eruptive magmatic processes re-timed using a non-isothermal approach to magma chamber dynamics

Rosi, M., & Sbrana, A. (1987). Phlegrean fields. Quaderni de la Ricerca Scientifica, 9(114).

Santacroce R, Cioni R, Marianelli P, Sbrana A, Sulpizio R, Zanchetta G, Joron JL (2008) Age and whole rock–glass compositions of proximal pyroclastics from the major explosive eruptions of Somma-Vesuvius: a review as a tool for distal tephrostratigraphy. J Volcanol Geotherm Res 177:1–18. https://doi.org/10.1016/j. jvolgeores.2008.06.009

Sinno, R. (1955). Studio geologico e petrografico della zona Monte Olibano-Pozzuoli. Tip. Guglielmo Genovese.

Smith, V. C., Isaia, R., & Pearce, N. J. G. (2011). Tephrostratigraphy and glass compositions of post-15 kyr Campi Flegrei eruptions: implications for eruption history and chronostratigraphic markers. Quaternary Science Reviews, 30(25-26), 3638-3660.